



**HAL**  
open science

# Exploring the Critical Zone Heterogeneity and the Hydrological Diversity Using an Integrated Ecohydrological Model in Three Contrasted Long-Term Observatories

J. Ackerer, S. Kuppel, I. Braud, S. Pasquet, Ophélie Fovet, A. Probst, Marie-Claire Pierret, Laurent Ruiz, T. Tallec, N. Lesparre, et al.

## ► To cite this version:

J. Ackerer, S. Kuppel, I. Braud, S. Pasquet, Ophélie Fovet, et al.. Exploring the Critical Zone Heterogeneity and the Hydrological Diversity Using an Integrated Ecohydrological Model in Three Contrasted Long-Term Observatories. *Water Resources Research*, 2023, 59 (12), pp.e2023WR035672. 10.1029/2023WR035672 . hal-04344295

**HAL Id: hal-04344295**

**<https://hal.science/hal-04344295>**

Submitted on 14 Dec 2023

**HAL** is a multi-disciplinary open access archive for the deposit and dissemination of scientific research documents, whether they are published or not. The documents may come from teaching and research institutions in France or abroad, or from public or private research centers.

L'archive ouverte pluridisciplinaire **HAL**, est destinée au dépôt et à la diffusion de documents scientifiques de niveau recherche, publiés ou non, émanant des établissements d'enseignement et de recherche français ou étrangers, des laboratoires publics ou privés.



Distributed under a Creative Commons Attribution - NonCommercial - NoDerivatives 4.0 International License

# Water Resources Research



## RESEARCH ARTICLE

10.1029/2023WR035672

### Key Points:

- The long-term critical zone (CZ) evolution controlling the regolith thickness strongly impacts the total water storage in watersheds, while the Quaternary geomorphological evolution influences the current hydrological partitioning and the separation of hydrologically active and inactive water storage
- Both internal watershed characteristics and external forcings, such as current atmospheric forcing and recent land use need to be considered to infer stream persistence and to understand hydrological diversity
- The observed hydrological diversity cannot be fully understood without considering a continuum of time scales in CZ evolution

### Supporting Information:

Supporting Information may be found in the online version of this article.

### Correspondence to:

J. Ackerer,  
julien.ackerer@orange.fr

### Citation:

Ackerer, J., Kuppel, S., Braud, I., Pasquet, S., Fovet, O., Probst, A., et al. (2023). Exploring the critical zone heterogeneity and the hydrological diversity using an integrated ecohydrological model in three contrasted long-term observatories. *Water Resources Research*, 59, e2023WR035672. <https://doi.org/10.1029/2023WR035672>

Received 26 JUN 2023

Accepted 18 NOV 2023

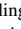


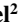

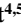
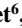



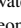

### Author Contributions:

**Conceptualization:** J. Ackerer, S. Kuppel  
**Data curation:** O. Fovet, A. Probst, M. C. Pierret, T. Tallec, S. Weill, C. Flechard, J. L. Probst

© 2023. The Authors.

This is an open access article under the terms of the [Creative Commons Attribution-NonCommercial-NoDerivs License](https://creativecommons.org/licenses/by-nc-nd/4.0/), which permits use and distribution in any medium, provided the original work is properly cited, the use is non-commercial and no modifications or adaptations are made.

## Exploring the Critical Zone Heterogeneity and the Hydrological Diversity Using an Integrated Ecohydrological Model in Three Contrasted Long-Term Observatories

J. Ackerer<sup>1</sup> , S. Kuppel<sup>2</sup> , I. Braud<sup>3</sup> , S. Pasquet<sup>4,5</sup> , O. Fovet<sup>6</sup>, A. Probst<sup>7</sup> , M. C. Pierret<sup>8</sup>, L. Ruiz<sup>6</sup>, T. Tallec<sup>9</sup> , N. Lesparre<sup>8</sup> , S. Weill<sup>8</sup>, C. Flechard<sup>6</sup> , J. L. Probst<sup>7</sup> , J. Marçais<sup>3</sup> , A. Riviere<sup>10</sup>, F. Habets<sup>11</sup>, S. Anquetin<sup>1</sup> , and J. Gaillardet<sup>12</sup> 

<sup>1</sup>Institut des Géosciences de l'Environnement, IGE, St Martin d'Hères, France, <sup>2</sup>Géosciences Environnement Toulouse, CNRS-IRD-UPS-CNRS, Toulouse, France, <sup>3</sup>INRAE, RiverLy, Villeurbanne, France, <sup>4</sup>Observatoire des Sciences de l'Univers, CNRS, ECCE TERRA, UAR 3455, Sorbonne Université, Paris, France, <sup>5</sup>CNRS, EPHE, UMR 7619 METIS, Sorbonne Université, Paris, France, <sup>6</sup>INRAE, Rennes, France, <sup>7</sup>Laboratoire Ecologie Fonctionnelle et Environnement, ENSAT, Castanet-Tolosan, France, <sup>8</sup>Institut Terre et Environnement de Strasbourg, ITES, Strasbourg, France, <sup>9</sup>Centre d'Etudes Spatiales de la Biosphère, CESBIO, Toulouse, France, <sup>10</sup>Centre de Géosciences Mines Paris, PSL, Paris, France, <sup>11</sup>Laboratoire de Géologie, CNRS UMR 8538, École Normale Supérieure, PSL University, IPSL, Paris, France, <sup>12</sup>Institut de Physique du Globe, IPGP, Paris, France

**Abstract** An integrated ecohydrological modeling approach was deployed in three long-term critical zone (CZ) observatories of the French CZ network (CZ Observatories—Application and Research) to better understand how the CZ heterogeneity modulates the water cycle within territories. Ecohydrological simulations with the physically based model EcH<sub>2</sub>O-iso constrained by a wide range of observations crossing several disciplines (meteorology, hydrology, geomorphology, geophysics, soil sciences, and satellite imagery) are able to capture stream water discharges, evapotranspiration fluxes, and piezometric levels in the Naizin, Auradé, and Strengbach watersheds. In Naizin, an agricultural watershed in northwestern France with a schist bedrock underlying deep weathered materials (5–15 m) along gentle slopes, modeling results reveal a deep aquifer with a large total water storage (1,080–1,150 mm), an important fraction of inactive water storage (94%), and relatively long stream water transit times (0.5–2.5 years). In the Auradé watershed, representative of agricultural landscapes of the southwestern France developed on molasse, a relatively shallow regolith (1–8 m) is observed along hilly slopes. Simulations indicate a shallow aquifer with moderate total water storage (590–630 mm), an important fraction of inactive water storage (91%), and shorter stream water transit times (0.1–1.3 years). In the Strengbach watershed, typical of mid-mountain forested landscapes developed on granite, CZ evolution implies a shallow regolith (1–5 m) along steep slopes. Modeling results infer a shallow aquifer with the smallest total water storage (475–575 mm), the shortest stream water transit times (0.1–0.7 years), but also the highest fraction of active water storage (18%).

**Plain Language Summary** Understanding how water is stored and released in landscapes is essential for predicting water availability in a changing world. It is of course driven by the local climate, but also by the landscape settings, from the vegetation to the belowground structure inherited from the geological history. In three intensively studied observatories across France, we used numerous field measurements and a numerical model of water-vegetation-subsurface interactions to better depict how differences between landscapes shape the water cycle. We found that the geological history determines how much water is stored in watersheds, through the thickness of water-holding rocks and soils. How this storage contributes to surface processes (including river flow) is modulated by more recent changes, from valley morphology and tectonics to agricultural practices and precipitation patterns. This study highlights that considering the continuity between long and short-term landscape processes is key to a detailed understanding of the water cycle.

## 1. Introduction

The critical zone (CZ) is defined as the superficial part of the Earth extending from the lower atmosphere to the unweathered, impermeable bedrock (US National Research Council, 2001). This thin layer hosts complex interfaces between the lithosphere and the atmosphere, shaped by geological forces (tectonic), external forces (solar energy), and biological forces (life processes). Most of the Earth's terrestrial living organisms inhabit the

**Formal analysis:** J. Ackerer  
**Funding acquisition:** I. Braud, F. Habets, S. Anquetin, J. Gaillardet  
**Investigation:** J. Ackerer, S. Pasquet  
**Methodology:** J. Ackerer, S. Kuppel, S. Pasquet, N. Lesparre  
**Project Administration:** I. Braud, F. Habets, S. Anquetin, J. Gaillardet  
**Resources:** I. Braud, S. Pasquet, O. Fovet, A. Probst, M. C. Pierret, L. Ruiz, T. Tallec, N. Lesparre, S. Weill, C. Flechard, J. L. Probst  
**Software:** J. Ackerer, S. Kuppel  
**Supervision:** I. Braud, F. Habets, S. Anquetin, J. Gaillardet  
**Validation:** J. Ackerer, S. Kuppel, I. Braud, O. Fovet, A. Probst, M. C. Pierret, L. Ruiz, T. Tallec, N. Lesparre, S. Weill, C. Flechard, J. L. Probst, J. Marçais, A. Riviere, F. Habets, S. Anquetin, J. Gaillardet  
**Visualization:** A. Probst, M. C. Pierret, L. Ruiz, J. Gaillardet  
**Writing – original draft:** J. Ackerer, S. Kuppel, I. Braud, S. Pasquet, O. Fovet, A. Probst, M. C. Pierret, L. Ruiz, T. Tallec, N. Lesparre, S. Weill, C. Flechard, J. L. Probst, J. Marçais, A. Riviere, F. Habets, S. Anquetin, J. Gaillardet

CZ, both modifying its structure and depending on its evolution at various time scales. Humans are no exception, and even if our ability to modify the CZ state outpaces that of other living species, our societies are inherently dependent on its integrity for fresh water supply, soil sustainability, and food production, among other things (Brantley et al., 2017; Chorover et al., 2011).

The last decades have witnessed a significant acceleration of global environmental changes, as anthropogenic impacts on Earth system functioning become more and more tangible and concerning (Aguilar et al., 2020; Steffen et al., 2015). However, this global trend driven by human activities does not have the same effects in all regions and within territories. One of the reasons is that atmospheric dynamics themselves do not uniformly change at regional scales (e.g., Strohmenger et al., 2022; Xie et al., 2015). Another important reason is also that the geological history and the geochemical evolution encountered across landscapes are very diverse (White et al., 2015). Tectonic, lithology, geomorphology, weathering depths, or soil properties: the heterogeneity of the solid part of the CZ may in particular modulate the hydrological functioning of watersheds and their responses to external forcings (Ackerer et al., 2020).

Developing a predictive model of the CZ evolution relevant within territories (i.e., CZ earthcasting; Goddérès & Brantley, 2013) faces the challenge of depicting CZ heterogeneity, understanding how it affects watershed functioning, and how it generates hydrological diversity at more regional scales. By hydrological diversity, we refer here to differences in water partitioning, water transit times, water storage dynamics, and stream persistence. Another key point is to better consider the effect of a specific long-term trajectory on short-term processes, such as linking geological and geochemical evolution to specific features of the water cycle. Making such advances requires additional efforts for developing integrated CZ models that are able to connect different CZ compartments, to link short and long timescales, and to consider energy and water fluxes in the vegetation-surface-soil-regolith continuum.

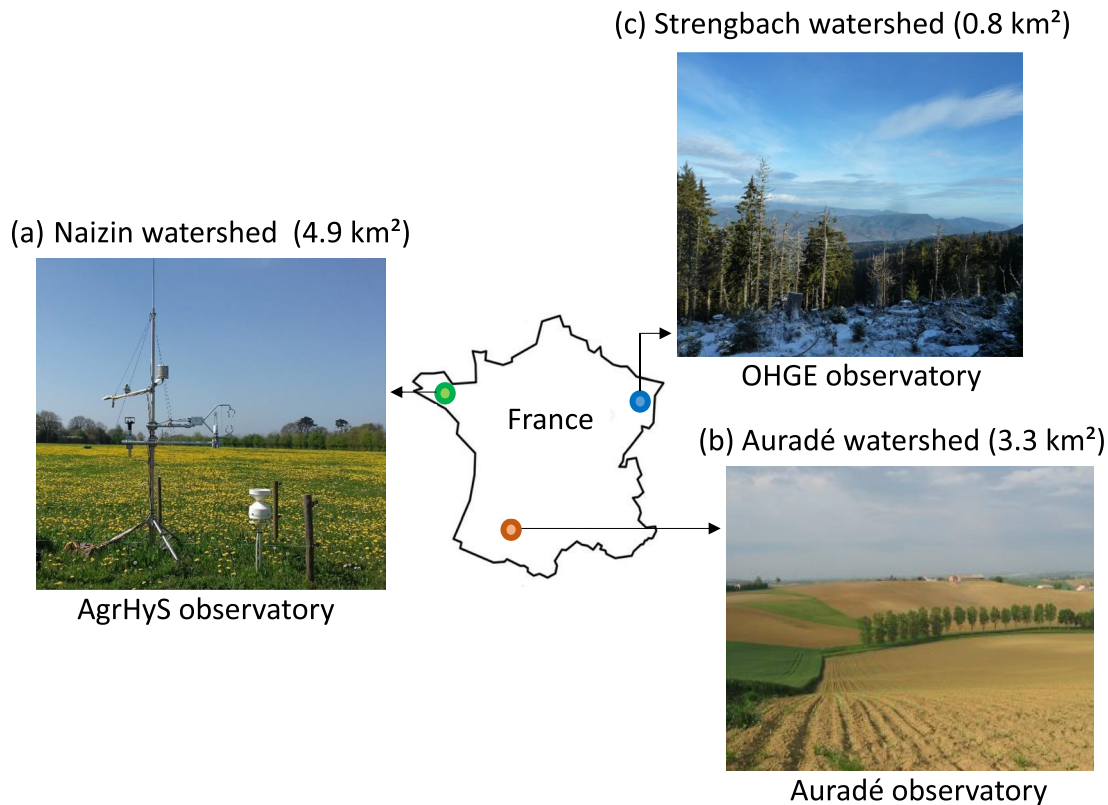
Recent efforts were made toward this goal and the complexity of integrated models has significantly increased over the last years (e.g., ATS model, Coon et al., 2020; Parflow model, Kuffour et al., 2020; Condon et al., 2020; RT-Flux-PIHM model, Bao et al., 2017; EcH<sub>2</sub>O model, Maneta & Silverman, 2013). Integrated modeling approaches allowed to capture the variability of hydrological processes along slopes (Tetzlaff et al., 2014), to evaluate the interplay between climate and geology in controlling water partitioning and transit times (Kuppel et al., 2020; Maxwell et al., 2016), to explore the impact of landscape heterogeneity on hydrochemistry (Ackerer et al., 2020; Li et al., 2017; Xu et al., 2022), and to test how these insights are sensitive to the chosen modeling scale and resolution (Shuai et al., 2022). However, one of the limitations of these integrated modeling approaches is the large number of observations required to constrain numerical simulations. Characterizing vegetation state, land use, hydrodynamic properties, or regolith thickness are commonly dependent on a simplified, calibrated parameterization of modeled domain, and this is particularly true when these models are deployed across several watersheds in comparative studies.

The French CZ network CZ Observatories—Application and Research (OZCAR; Braud et al., 2020; Gaillardet et al., 2018) provides the opportunity to foster a synergy between observations and models across a gradient of CZ observatories. These CZ observatories (CZO) are regionally based, instrumented sites where multidisciplinary and systemic approaches are deployed to study the CZ as a whole system. The wide range of observations collected in the OZCAR network (Braud et al., 2020) especially allows to constrain part of the heterogeneity for many parameters required by integrated models, including parameters describing vegetation state, land use, or regolith thickness.

In this study, we propose a new step in observation-model interactions by deploying an integrated ecohydrological modeling of the water cycle in three contrasted observatories from the OZCAR network. Our major objectives are (a) to characterize CZ heterogeneity at regional scales through a multi-site study and to explore how this heterogeneity generates hydrological diversity, (b) to understand how this CZ heterogeneity interacts with climate and land use in controlling hydrological processes, water transit time, and water storage dynamics within watersheds, and (c) to explore how different trajectories of long-term evolution explain CZ heterogeneity and hydrological diversity.

## 2. Study Observatories

This study is based on the data collected within three CZOs of the OZCAR network in France: AgrHyS (located in Brittany, north-west of France; Figure 1a; Fovet et al., 2018), Auradé (located in Gers, south-west of France; Figure 1b; Probst & Probst, 2022) and OHGE (“Observatoire HydroGéochimique de l’Environnement”, located



**Figure 1.** Location of the three critical zone observatories investigated in this study with (a) the Naizin watershed in the Brittany region, northwestern France (AgrHyS observatory), (b) the Auradé watershed in the Gers region, southwestern France (Auradé observatory), and (c) the Strengbach watershed in the Vosges mountains, northeastern France (OHGE observatory). These observatories provide 30 years of long-term and multidisciplinary data in contrasting contexts and are all part of the French critical zone OZCAR research infrastructure (Braud et al., 2020; Gaillardet et al., 2018). Photos are from the database of AgrHyS (a), Auradé (b), and OHGE (c) observatories.

in Vosges Mountains, north-east of France; Figure 1c; Pierret et al., 2018). These observatories were designed to monitor the evolution of three watersheds during more than 30 years: the Naizin watershed (AgrHyS observatory, 4.9 km<sup>2</sup>; Figure 1a), the Auradé watershed (also referred as Montoussé watershed; Auradé observatory; 3.3 km<sup>2</sup>; Figure 1b) and the Strengbach watershed (OHGE observatory; 0.8 km<sup>2</sup>; Figure 1c). Each watershed presents specific characteristics in terms of geology, climate, land use, and anthropogenic impacts. An overview of their general features is provided in Table 1, and the most significant points are detailed in the following.

The Naizin watershed is characterized by a plain landscape with a low mean elevation ( $\approx 110$  m), mostly flat (elevation range  $\approx 40$  m) with gentle slopes ( $< 5\%$ ). The local climate is typical of a temperate oceanic climate (Table 1; Gascuel-Oudoux et al., 2010). The bedrock is a fractured and fissured Brioverian schist (age  $\approx 550$  Myr), a metasedimentary rock frequently encountered in the Brittany region of northwestern France. A permanent, unconfined, and relatively deep aquifer has developed in the weathered schist over the entire watershed (Gascuel-Oudoux et al., 2010). Soils are silty-loams (0.5–1.5 thick), rich in organic matter, and well drained on the upper parts of hillslopes (cambisols) but more hydromorphic along the river network (Albeluvisols). The current land use is strongly dominated by the intensive farming with diverse crop rotations, which usually include wheat and maize crops and grasslands. A synthetic overview of the observation and research works conducted in the Naizin watershed is available in Fovet et al. (2018).

The Auradé watershed is characterized by a hilly landscape with a low mean elevation ( $\approx 220$  m), moderate reliefs ( $\approx 80$  m), and steeper slopes (5%–20%). Its current climate is of oceanic type and exhibits both Mediterranean and warm-oceanic influences (Table 1; Ponnou-Delaffon et al., 2020). The bedrock is an impervious Miocene molasse (age  $\approx 20$  Myr), a sedimentary rock commonly found in the Gers region of southwestern France. A shallow, unconfined, and limited aquifer has developed in the weathered molasse and especially in colluvial deposits and sandy lenses located on bottomlands and/or at mid-slopes. Soils are relatively impervious clay-rich



**Table 1**  
*Localization and General Overview of the Three Critical Zone Observatories Investigated in This Study*

	Naizin watershed	Auradé watershed	Strengbach watershed
Critical zone observatory	AgrHyS	Auradé	OHGE
Localization	48.00°N, 2.83°W	43.56°N, 1.065°E	48.21°N, 7.20°E
Area (km <sup>2</sup> )	4.9	3.3	0.8
Elevation (m)	130–100	260–180	1,100–850
Climate type	Oceanic-temperate	Mediterranean-oceanic	Mountain-temperate
Mean annual temperature (°C)	11	14.5	6.5
Mean annual precipitation (mm)	840	650	1,400
Mean annual runoff (mm)	325	100	800
Mean annual evapotranspiration (mm)	515	550	600
Bedrock type	Brioverian schists	Miocene molasse	Hercynian granite
Soil type	Silty-loam soils	Argillaceous soils	Brown acidic soils
Vegetation type	Wheat crop	Wheat crop	Spruces
	Maize crop	Sunflower crop	Beeches
	Grassland	Grassland	
Land use	Deciduous trees	Deciduous trees	
	Agricultural crops	Agricultural crops	Forest
	Grassland	Grassland	
	Buildings and farms	Buildings and farms	
Anthropogenic impacts	Woods	Woods	
	Agriculture	Agriculture	Forestry
	Farming	Farming	Forest management
	Deforestation	Deforestation	

*Note.* Climatic averages given in the table are long-term averages calculated over the last 30 years.

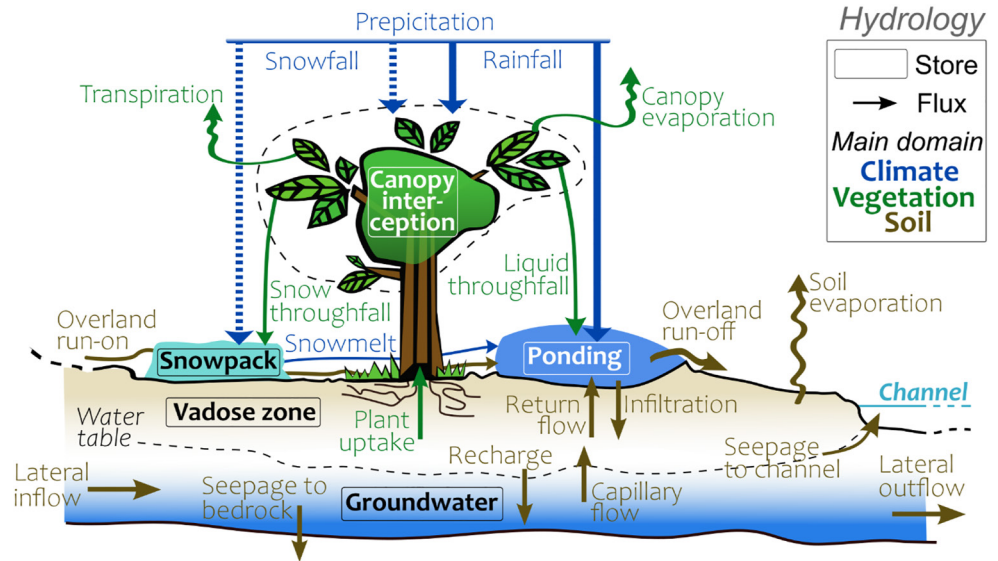
soils (calcaric cambisol type, 0.5–1.5 m thick), poor in organic matter, with colluvial deeper soils deposited at the bottom of hillslopes. The current land use is dedicated to intensive agriculture, with mainly wheat and sunflower crops in rotation, farms, and few grasslands (Perrin et al., 2008). A synthetic overview of the observation and research activities conducted in the Auradé watershed is available in Probst and Probst (2022).

The Strengbach watershed is characterized by a mid-mountain landscape with an intermediate mean elevation ( $\approx 1,000$  m), significant reliefs ( $\approx 350$  m), and much steeper slopes (10%–45%). Its current climate is typical of a mountain-temperate climate (Table 1; Strohmenger et al., 2022). The bedrock is a fractured and partially hydrothermally overprinted Hercynian granite ( $\approx 315$  Myr), one of the principal crystalline rock of the Vosges Mountains. The groundwater reservoir of the watershed is distributed between soils, regolith, and more or less fractured granite (Ackerer et al., 2021; Chabaux et al., 2023; Ranchoux et al., 2021), resulting in an important spatial variability of water storage. An unconfined and shallow aquifer has also developed in a saturated area located nearby the watershed outlet. Soils are brown acidic soils (alocrisol to ochreous podzolic soil types, 0.5–1 m thick), sandy and well drained, except in the saturated zone where poorly drained soils are present. The current land use is dominated by spruce ( $\approx 80\%$ ) and beech ( $\approx 20\%$ ) forested plots. Anthropogenic impacts are limited to forest management, climate change, and atmospheric deposition. A general overview of the observation and research works conducted in the Strengbach watershed is available in Pierret et al. (2018).

### 3. Methods

#### 3.1. The Ecohydrological Model EcH<sub>2</sub>O-Iso

An integrated modeling approach of the water cycle was developed in the three above-mentioned watersheds with the ecohydrological model EcH<sub>2</sub>O-iso (Kuppel et al., 2018b; Maneta & Silverman, 2013). EcH<sub>2</sub>O-iso is a



**Figure 2.** Schematic representation of the water storage compartments and of the main hydrological processes considered by the spatially distributed and physically based ecohydrological model  $Ech_2O$ -iso (figure adapted from Kuppel et al. (2018b)). Blue, green, and brown colors refer to climate, vegetation, and soil-groundwater domains respectively. Arrows show hydrological fluxes associated to the main hydrological processes and rectangles correspond to water storage compartments considered by  $Ech_2O$ -iso.

physically based, spatially distributed model solving energy and water fluxes in the vegetation-surface-soil-regolith continuum (Figure 2; Kuppel et al., 2018a; Smith et al., 2022). Its original development was motivated by finding a middle ground between catchment detailed hydrologic models and land surface models simulating energy balance and vegetation dynamics (Lozano-Parra et al., 2014; Maneta & Silverman, 2013). We provide below an overview of the processes simulated in the model regarding hydrology and energy transfers and some of the associated equations; for a more in-depth description, the reader is referred to Maneta and Silverman (2013) and the appendices of Kuppel et al. (2018a).

The spatial domain of  $Ech_2O$ -iso consists of regular cells derived from the digital elevation model (DEM) of the study area. Atmospheric inputs are for each time step: precipitation, air temperature at 2 m (average, maximum, and minimum), relative air humidity, wind speed, incoming shortwave radiation, and downward longwave radiation at the top of the canopy. Vegetation interception is calculated using an interception storage capacity proportional to the leaf area index (LAI) which is emptied via direct evaporation. When the interception storage is full exceeding precipitation makes up for throughfall. The variation of canopy storage is expressed by:

$$\frac{dC_{stor}}{dt} = P_r + P_s - TF - E_c \quad (1)$$

where  $C_{stor}$  is the current canopy water storage (m),  $P_r$  is the rainfall ( $m \cdot s^{-1}$ ),  $P_s$  is the snowfall ( $m \cdot s^{-1}$ ),  $TF$  is throughfall ( $m \cdot s^{-1}$ ), and  $E_c$  is the evaporation of water intercepted by the canopy ( $m \cdot s^{-1}$ ; Maneta & Silverman, 2013). The partition of precipitation and throughfall between rain and snow is determined from the air temperature and a snow-rain transition temperature threshold ( $T_{rs} = 2^\circ C$ ). Liquid water from snowmelt or rainfall feeds surface ponding, which can infiltrate into the upper soil following a Green and Ampt approximation of the Richards equation (Maneta & Silverman, 2013):

$$I_f = K_s^{L1} \cdot A_{vh} \left[ \frac{\psi_{ae} (1 - S_\theta^{L1}) \eta}{\theta_{L1} \cdot d} + 1 \right] \quad (2)$$

where  $I_f$  is the infiltration rate ( $m \cdot s^{-1}$ ) into the first of the three subsurface model layers (see below), where  $K_s^{L1}$  is the saturated lateral hydraulic conductivity ( $m \cdot s^{-1}$ ),  $A_{vh}$  is the vertical-to-horizontal anisotropy ratio,  $\psi_{ae}$  is the soil-air entry pressure (m),  $\eta$  is the effective porosity,  $\theta_{L1}$  is the volumetric water content ( $m^3 \cdot m^{-3}$ ),  $d$  is the layer depth (m), and  $S_\theta^{L1}$  is the relative saturation ( $(\theta_{L1} - \theta_r) / (\eta - \theta_r)$ ) where  $\theta_r$  is the residual volumetric water content

( $\text{m}^3 \cdot \text{m}^{-3}$ ). The non-infiltrated surface water is routed to the neighboring cell as surface runoff. This overland runoff, just like channel flow and subsurface lateral flow, follows the local drainage direction determined using D8 flow direction to the steepest downslope neighbor with the input DEM map: it can infiltrate along its path or generate further runoff until it reaches a channel cell. The channel flow is described using a 1D solution of the kinematic wave equation with a power function relating cross-section flow area to stream discharge (Kuppel et al., 2018a).

One of the interest of EcH<sub>2</sub>O-iso is also its ability to consider a part of the complexity of the CZ vertical structure. The subsurface domain comprises three layers that can be delimited depending on the application. The first layer, where ponding water infiltrates, is the only one where the direct evaporation of water occurs and is here representing the topsoil. The second layer is here representing the deeper soil where most of the plant roots are present in addition to the topsoil. In this study, the third layer corresponds to the weathered bedrock (the lower regolith).

Subsurface water flow assumes that only water above field capacity can flow to deeper layers or laterally into adjacent cells, and these two components are computed separately as 1D flows to increase computational efficiency. This gravitational water flowing to the layer below is determined by linearized unsaturated hydraulic conductivity based on effective saturated hydraulic conductivity, anisotropy, and volumetric water content (Kuppel et al., 2018a). Lateral subsurface flow is limited to the third layer, where gravitational flux per unit width is taken proportional to the saturated hydraulic conductivity and slope (assumed equal to the DEM-derived surface slope). Seepage of this groundwater in the stream occurs in channel cells, based on an exponential decay function of gravitational storage and hydraulic conductivity (Maneta & Silverman, 2013) as:

$$q_{\text{chan}} = K_s^{L3} h_g (1 - \exp(-b \cdot h_g)) \quad (3)$$

where  $q_{\text{chan}}$  is the rate of water transfer from the subsurface system to the channel ( $\text{m} \cdot \text{s}^{-1}$ ),  $K_s^{L3}$  is the saturated lateral hydraulic conductivity of the regolith ( $\text{m} \cdot \text{s}^{-1}$ ),  $b$  is a coefficient controlling the resistance to flow at the subsurface-channel interface ( $\text{m}^{-1}$ ), and  $h_g$  is the gravitational water height in excess of field capacity  $\theta_{fc}$ :

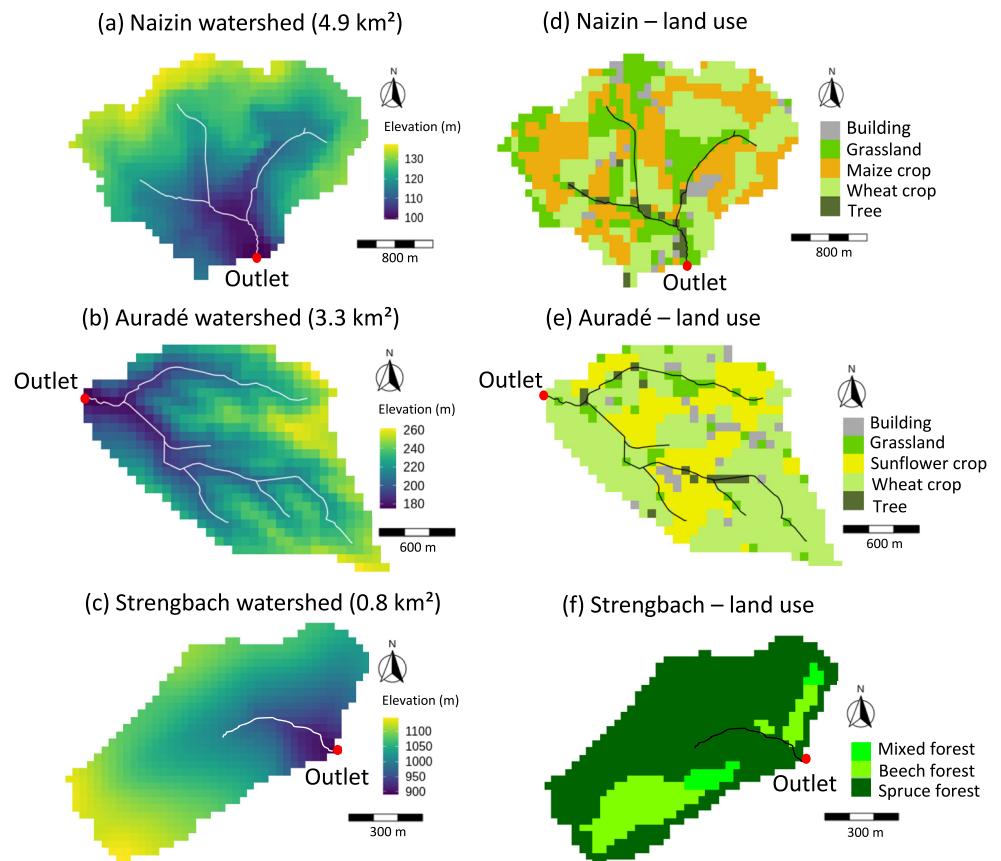
$$h_g = (\theta_{L3} - \theta_{fc}) \cdot d_{L3} \quad (4)$$

where  $\theta_{L3}$  and  $d_{L3}$  are the volumetric water content ( $\text{m}^3 \cdot \text{m}^{-3}$ ) and depth (m) of the third subsurface layer, respectively. The rest of the moisture below field capacity is retained in the subsurface and only removed by evapotranspiration (ET) processes.

The three components of the ET (canopy evaporation, soil evaporation, plant transpiration) are separately quantified through solving the energy balance closure at canopy and surface levels. The canopy-level calculation explicitly couples the radiation budgets with sensible heat, latent heat from evaporative losses (interception and root uptake), atmospheric vapor pressure deficit, and subsurface water availability to plants. The latter, and the resulting root water uptake profile in the subsurface layers, is constrained by an exponential root profile specified for each plant type (Kuppel et al., 2018a). The other main vegetation control on water and energy transfer is through canopy conductance, which uses a Jarvis-type multiplicative formulation using LAI and efficiencies functions for vapor pressure deficit (accounting for stomatal closure in dry conditions), plant-available subsurface moisture, solar radiation, and air temperature. The surface-level energy balance distributes the available energy between ground heat flux, latent heat of snow melt, heat flux in the snowpack, latent heat of soil evaporation, sensible heat, and net radiation.

As the model can consider several land cover types (vegetation species or bare soil) on each grid cell, the computation of energy balance, evaporative fluxes, and canopy-level water storage is made for each land cover and weighted by the fraction occupied. While the vegetation state can be dynamically calculated by EcH<sub>2</sub>O-iso using a carbon allocation module with different growth schemes for ligneous and herbaceous species (Lozano-Parra et al., 2014; Maneta & Silverman, 2013), this feature is here disconnected as LAI was taken as an external forcing from observations (Section 3.2). As a result, the dynamic interactions between vegetation, atmospheric conditions, and subsurface water storage are here limited to energy balance, interception, and ET processes, nonetheless reflecting the spatial variability of land cover types considered in this study (Section 3.2 and Figure 3).

Finally, EcH<sub>2</sub>O-iso allows for tracking conservative tracers (stable isotopes <sup>2</sup>H, <sup>18</sup>O, and chloride) and water ages (since arrival in precipitation, used in this study) in the various water stores and fluxes simulated (Douinot et al., 2019; Kuppel et al., 2018b). The flux-store approach adopted locally applies full-mixing mass balance



**Figure 3.** Geomorphological and land use features considered by the ecohydrological modeling within the three watersheds. Subplots (a–c) show size scale, elevation, stream network, and outlet location for the Naizin, Auradé, and Strengbach watersheds. Elevation scales are adapted for each watershed for visibility purpose. Subplots (d–f) show the land use considered by the model EcH<sub>2</sub>O-iso for the three watersheds. Each square represents a cell in the spatially distributed modeling. For Naizin and Auradé watersheds that are concerned by crop rotations the land use is shown for the year 2013.

equations at each sub-time step when water is exchanged between CZ compartments, effectively propagating the signature of interest across the catchment without requiring additional parameters. This simplicity makes the computation efficient while still providing space and time-varying estimates of tracers and water ages at the landscape scale. Note that preferential transit of water (e.g., preferential flow or pore space selection in root uptake, e.g., Sprenger & Allen, 2020) is not accounted for at the local scale: outgoing fluxes in EcH<sub>2</sub>O-iso have the same fully mixed signature as their feeding pools (see Kuppel et al., 2020 for a further discussion).

Overall, EcH<sub>2</sub>O-iso is a model designed for the integrated modeling of the CZ as it enables to consider different CZ compartments (i.e., lower atmosphere, vegetation, soil, and groundwater zone), to link a variety of processes operating at different timescales (i.e., rapid runoff or ET processes; slow groundwater flow; Figure 2), while also linking water storage and flux dynamics to water transit times in the associated CZ compartments and outflow (Kuppel et al., 2020). Its parsimonious construction also ensures reasonable computation times for multi-site studies demanding a large number of simulations.

### 3.2. Observation and Available Data

An important effort was made to consider a large range of observations for constraining the integrated CZ modeling performed by EcH<sub>2</sub>O-iso. The period from 2006 to 2014 was selected for conducting and evaluating ecohydrological simulations, as this time window offers the best data availability in the three CZOs, especially for the documentation of land use in agricultural watersheds.

The atmospheric forcings rely on in situ observations gathered by local weather stations implanted in the three observatories (data available for air temperatures, precipitation, wind speed, relative air humidity, and incoming



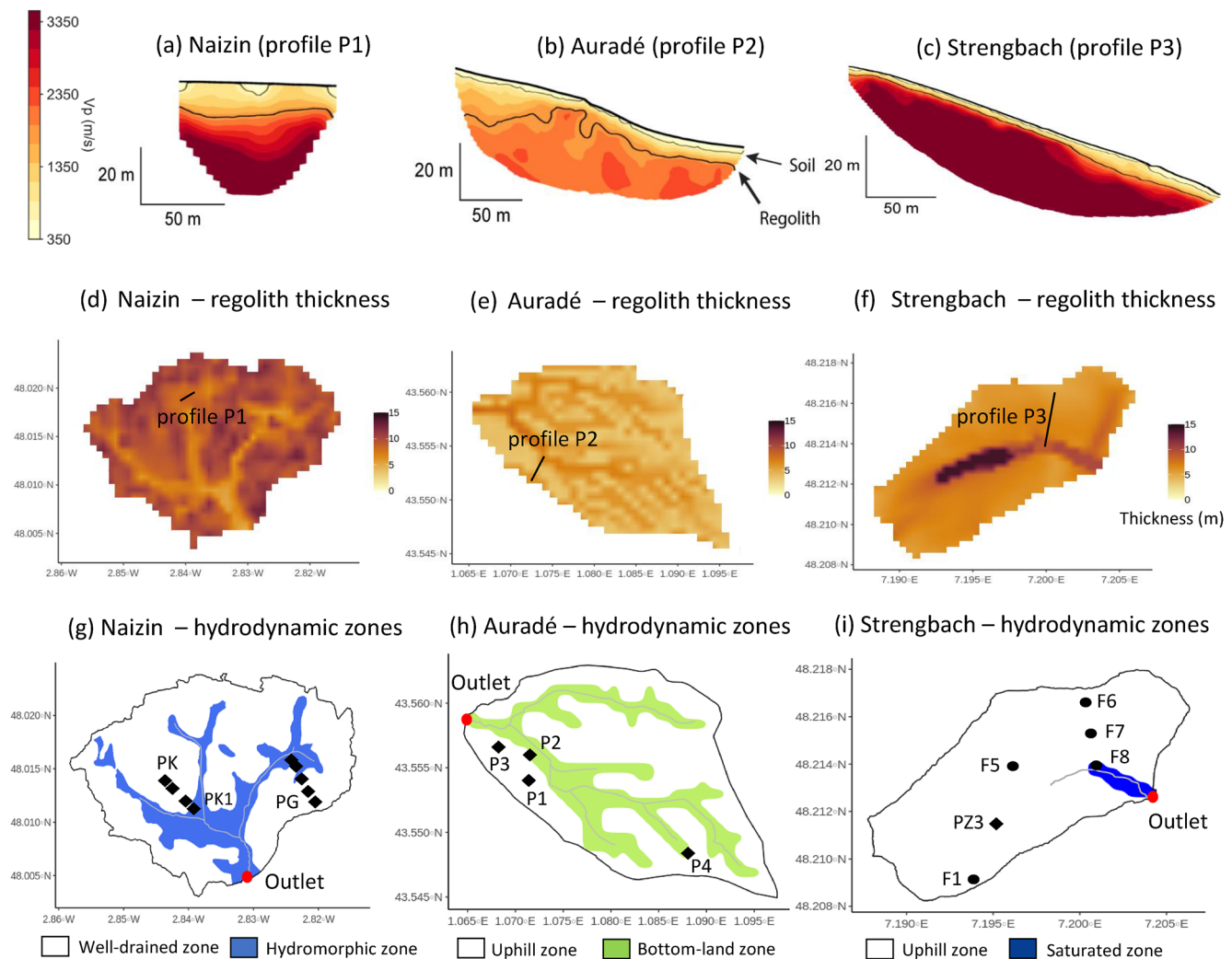
shortwave radiation; Fovet et al., 2018; Pierret et al., 2018; Probst & Probst, 2022; Strohmenger et al., 2022). Given the small size of the three watersheds (0.8–4.9 km<sup>2</sup>), we assumed that the atmospheric variables are spatially homogeneous within each watershed and we did not use downscaling techniques with remote sensing or reanalyses data sets, with one exception. As downward longwave radiation is not routinely measured by local weather stations, we used the hourly outputs from the SAFRAN reanalysis of the French meteorological center (Habets et al., 2008; Vidal et al., 2010). Atmospheric variables were mostly available at the hourly resolution during the study period, or were aggregated at this resolution when data had a shorter time step.

Land use was determined from mapping campaigns using agricultural maps and satellite images, with 1 and 8-m spatial resolution, respectively (Ferrant et al., 2014, 2016; Keller et al., 2023; Viaud et al., 2018). In the case of the Naizin and Auradé watersheds that are dominated by intensive agriculture, we distinguished land use and land cover classes between buildings and farms, grasslands, woodlands, and winter crops (wheat) and spring crops (maize in Naizin or sunflower in Auradé) with respect to sowing and harvesting dates (Figure 3). Buildings, grasslands, and woodlands are considered as perennial over the simulation period while we assumed a simple year-to-year rotation between winter and spring crops. In the forested Strengbach watershed populated by spruce trees (mainly *Piceas abies* L., 80%) and beech trees (*Fagus sylvatica* L., 20%; Pierret et al., 2018), we used patches dominated by one species or the other, but mixed forest cover is also considered (Figure 3). This land use configuration was supposed constant in this watershed due to the stability of the forest type on the simulation time window.

LAI used to constrain the simulated vegetation state (see Section 3.3) was derived from in situ LAI measurements or from satellite images (Ferrant et al., 2014; Pierret et al., 2019). In agricultural watersheds such as Naizin and Auradé, the seasonal patterns of LAI strongly differ between plant types (Beaujouan et al., 2001). Winter and spring crops show a progressive LAI increase during their respective growing seasons (in early or late spring), followed by a plateau (centered in late spring or summer), and an abrupt LAI decrease during their respective harvest period (in summer or fall; Ferrant et al., 2016). Woodlands and grasslands show more progressive LAI variations with lower values in winter and higher values in summer. In the forested Strengbach watershed, there is marked contrast between the evergreen spruce trees showing moderate annual LAI variations and the deciduous beech trees characterized by large LAI variations between a short summer and a long period with no leaves (Pierret et al., 2019). Direct observations of ET fluxes from eddy covariance flux towers were also available in Naizin over a grassland plot (AgrHyS/CRITEX site; Fovet et al., 2018), to be compared with the summed simulated fluxes of soil evaporation, plant transpiration, and evaporated canopy interception. Here we use measurements made in 2017 although it does not overlap the simulated time period (see Section 3.3), as no eddy-covariance data was available in Naizin before then. In Auradé, eddy-covariance ET fluxes were available in 2013–2014 near the eastern part of the watershed over wheat or sunflower patches, for direct comparison with ecohydrological simulations (OSR SO/ICOS FR-Aur site; Ceschia & Tallec, 2022; Tallec et al., 2013).

Observations of the weathered material thickness gathered from previous studies (in depth profiles, boreholes, piezometers; Ackerer et al., 2021; Lesparre et al., 2020; Molénat et al., 2013; Pasquet, 2019; Trochon et al., 2023) and estimates derived from geophysical measurements were used to map the regolith thickness within the three watersheds. Geophysical measurements consist of seismic refraction tomography (SRT) data collected at each site to characterize the subsurface structure along hillslopes (more details on the SRT method are given in Supporting Information S1). This method has shown its effectiveness to map the architecture of the CZ in various geological settings (Befus et al., 2011; Flinchum et al., 2022; Pasquet et al., 2022). Observations were mainly focused along 2D transects extending from hilltops to valley floors (Figures 4a–4c). This strategy aims at capturing thickness variability due to erosion, transport, and deposition processes that are strongly controlled by slopes. These observations were then extrapolated to the whole watersheds based on a calculation of the topographic wetness index as a proxy of distance to stream network (TWI, Sørensen et al., 2006). The generated maps allow to consider the spatial variability of regolith thickness at the first order (Figures 4d–4f), in the prospect of taking into account the heterogeneous water storage capacity in the underlying aquifers.

Soil maps were derived from field sampling and processed to define the main hydrodynamic zones (Fovet et al., 2018; Gascuel-Oudoux et al., 2010; Lesparre et al., 2020; Probst & Probst, 2022; Weill et al., 2019; Figure 4). Hydrodynamic contrasts mostly appeared between upslope and downslope domains in the three watersheds. In Naizin, an uphill and well-drained zone contrasts with a downhill and more hydromorphic area along the stream network (Figure 4g). Low-permeability, clay-rich soils dominate the whole watershed in Auradé. There, colluvium deposits and sandy lenses are however present in the valley bottoms and on some hillslopes, defining a



**Figure 4.** Maps of geophysical transects, regolith thicknesses, and hydrodynamic zones over the three watersheds. Subplots (a–c) show pressure-wave velocity ( $V_p$ ) models obtained from seismic refraction tomography data collected in Naizin (a), Auradé (b), and Strengbach (c) watersheds. Soil and regolith boundaries are defined with  $V_p$  velocity thresholds of 700 and 1,400 m/s, respectively (Pasquet et al., 2022). Regolith thicknesses estimated along these transects are approximately 10–13 m in Naizin, 3–9 m in Auradé, and 2–5 m in the Strengbach. Subplots (d–f) provide the interpolated regolith thicknesses derived both from the observations gathered from boreholes, piezometers and from the geophysical measurements conducted in the watersheds. Geophysical transects are shown by black lines on maps. The depth scale is identical in the three subplots to highlight the major differences between the three watersheds. Subplots (g–i) show the main hydrodynamic zones considered in the ecohydrological modeling for the Naizin, Auradé, and Strengbach watersheds. Black diamonds and circles provide location of piezometers and boreholes, respectively.

zone where hydraulic conductivities are higher in the regolith compared to the soil (Figure 4h). In the Strengbach watershed, most of soils are well drained on crests and along slopes except in a saturated zone nearby the outlet.

### 3.3. Modeling Set Up

Numerical simulations were performed at the hourly resolution from January 2006 to December 2014, with spatial domains tailored for each watershed. The DEMs of the three watersheds were used to delineate domain boundaries and to consider their key geomorphological features (elevation, slopes, local drainage direction). The initial DEMs resolution available for the Strengbach (50 cm), Auradé (5 m), and Naizin (25 m) watersheds were aggregated to a gridded model domain at 75 m resolution for Naizin and Auradé watersheds and 33 m resolution for the Strengbach watershed. This allows for a similar number of grid cells (600–800) between the three simulated domains, with comparable and reasonable computation times at hourly resolution (~30 min per simulation).

We minimized the number of parameters to be manually calibrated by using as much as possible field observations as detailed in the above section (soil and regolith thicknesses, LAI seasonal dynamics, hydrodynamic

zones, and so on). The depth of whole hydrological domain of EcH<sub>2</sub>O-iso was defined by following maps of regolith thickness (Figures 4d–4f). Stream channel widths were assumed constant in the three watersheds (1 m). Vegetation parameters controlling rooting depth, stomatal conductance (maximum, dependence on vapor pressure deficit and light) and vegetation albedo were selected from previous studies and spatialized following land cover maps (Figure 3). In agricultural watersheds, we assumed that grid cells with buildings and farms are impervious and only generate runoff to adjacent cells. Calibration was used for total porosity, saturated hydraulic conductivity, and subsurface-channel seepage conductance as these parameters could not be documented at the watershed scale. Spatial heterogeneity was considered by vertically distinguishing the three model vertical layers (i.e., superficial soil, deeper soil, and regolith), and laterally adjusting one set of parameters per hydrodynamic zone (Figure 4). A summary of the main numerical parameters considered in the ecohydrological simulations performed with the model EcH<sub>2</sub>O-iso is provided in the supplementary materials (Table S1).

Calibration was carried out by targeting the best possible fit to stream water discharge at the outlets, piezometric levels along slopes, and ET fluxes measured by eddy covariance flux towers. Considering a diverse database informing about the state of different CZ compartments through evaluating these different outputs is essential to aim at a meaningful parametrization of such physically based models, by reducing the risk of equifinality (Kuppel et al., 2018a; Larsen et al., 2016; Maneta et al., 2007). Model-data fit was quantified using the Kling-Gupta Efficiency coefficient (KGE; Gupta et al., 2009) and root mean square errors (RMSE).

The first year of simulation (2006) was looped five times and used as a spin-up period and to reach a stability of the initial hydrological states. The model calibration period then extended from 2007 to 2012, just after the model spin-up phase (2006). Without changing any more model parameters, the model evaluation period focused on years 2013–2014, at the end of the simulation period. This time window was selected for the final modeling evaluation due to large range of data available for comparison with modeling results. The model ability to capture the main characteristics of the water cycle was evaluated by comparing simulated and observed stream water discharges, piezometric levels, and ET fluxes in 2013–2014. The quality of the fits was then assessed for this evaluation period by using KGE and RMSE values.

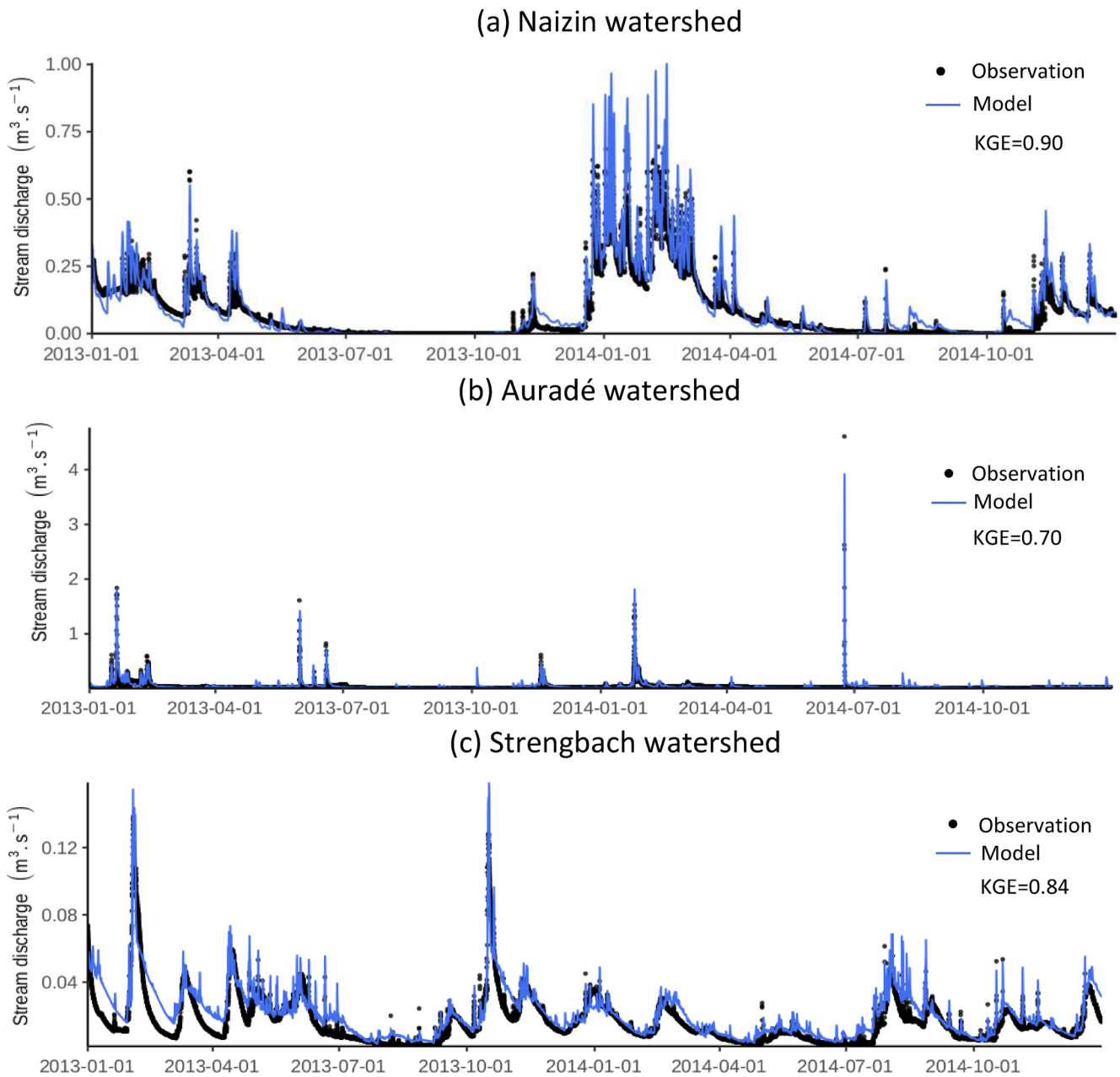
### 3.4. Calculation of Water Storage Dynamics

The total water storage in each watershed was calculated at a daily time step by taking the sum of all water storage components from the different CZ compartments as:

$$S = S_{\text{sub}} + S_{\text{swe}} + S_{\text{sur}} + S_{\text{veg}} \quad (5)$$

with  $S$  the total water storage in the CZ (expressed in water height equivalent, m),  $S_{\text{sub}}$  the water storage in the subsurface including soil water and groundwater (m),  $S_{\text{swe}}$  the water storage in the snowpack (snow water equivalent; m),  $S_{\text{sur}}$  the water storage in the surface ponding (m) and  $S_{\text{veg}}$  the water storage in the canopy (vegetation interception, m). In parallel, the daily variation of this total water storage ( $\Delta S$ ) was calculated in each watershed. Seasonal dynamics of the total water storage can be analyzed by simultaneously representing  $S$  and  $\Delta S$  variations in  $S$ - $\Delta S$  diagrams (Maneta et al., 2018). We conducted such analysis over the 2007–2014 time window, including both calibration and evaluation periods, to obtain multiyear trends of total water storage dynamics in the three watersheds. In addition, relative variations of the total water storage can be determined for a water year by normalizing the daily  $S$  values by the storage at the beginning of the water year (i.e., 1 October; normalized water storage is named  $S_{\text{normalized}}$ ). Interpretation of  $S_{\text{normalized}}$ - $\Delta S$  diagrams allows to determine the fraction of total water storage being mobilized under the observed climatic conditions and given the CZ characteristics.

For a deeper interpretation, the total water storage can be separated into hydrologically active and hydrologically inactive water storage. The hydrologically active water storage ( $S_a$ ) generates stream water discharges by being connected to stream network and is accessible to ET processes while the inactive water storage ( $S_i$ ) does not (Dralle et al., 2018; Maneta et al., 2018). One interesting approach to distinguish  $S_a$  and  $S_i$  is to perform synthetic simulations with precipitation set to zero (Maneta et al., 2018). With no precipitation, the hydrologically active storage is progressively depleted by outflows and the total water storage evolves following a drying trajectory until reaching a no-flux and passive state. The water storage remaining at the no-flux state represents the inactive water storage of the watershed. In our study, we performed synthetic simulations by succeeding usual ecohydrological simulations with unchanged precipitation (over the 2007–2012 hydrological years) with one full



**Figure 5.** Hourly stream discharge in 2013–2014 at the outlets of (a) Naizin, (b) Auradé, and (c) Strengbach watersheds. Black points represent observations and blue lines represent modeling results, with corresponding model-data Kling-Gupta Efficiency (KGE) values.

hydrological year with precipitation set to zero (over the hydrological year 2013–2014).  $S_{\text{normalized}}-\Delta S$  diagrams can then be used to visualize drying trajectories, to position the no-flux state and to determine fractions of hydrologically active and inactive water storage.

## 4. Results and Model Evaluation

### 4.1. Stream Water Discharges

Ecophysiological simulations are able to reproduce the stream water discharges at the outlets of the three watersheds over the years 2013–2014 (Figure 5). The best model-data fits are obtained for Naizin (Figure 5a, KGE = 0.90), followed by the Strengbach (Figure 5c, KGE = 0.84) and Auradé (Figure 5b, KGE = 0.70). In



Naizin, water discharges show a strong seasonality with a long period of low flow in summer ( $Q \approx 0.01 \text{ m}^3 \cdot \text{s}^{-1}$ ) and much higher flow rates in winter ( $Q \approx 0.2 \text{ m}^3 \cdot \text{s}^{-1}$ , sometimes reaching  $Q \approx 0.75 \text{ m}^3 \cdot \text{s}^{-1}$ , Figure 5a), although we note that the simulations tended to overestimate peak flows during the wet winter of 2013–2014. The stream frequently dries up in summer while few thunderstorms may generate important but brief increases in flow. In Auradé, stream discharge is more intermittent, without a comparable seasonality (Figure 5b). Stream flow is low for most of the year ( $Q \approx 0.01 \text{ m}^3 \cdot \text{s}^{-1}$ ), with short periods of more sustained flow rates in winter ( $Q \approx 0.1 \text{ m}^3 \cdot \text{s}^{-1}$ ). The most significant characteristics of this watershed is the occurrence of flash floods (up to  $Q \approx 1 \text{ m}^3 \cdot \text{s}^{-1}$ ) generated by oceanic depressions or thunderstorms in late spring (May–June) or in summer (July–August), which are sometimes underestimated in simulations (e.g., peak flow in June 2014). In the Strengbach, stream discharge shows a certain seasonality with higher flows in winter ( $Q \approx 0.1 \text{ m}^3 \cdot \text{s}^{-1}$ ) and yearly minima found in summer ( $Q \approx 0.01 \text{ m}^3 \cdot \text{s}^{-1}$ ; Figure 5c). One of the watershed's specificity is the presence of snow in winter with a highly variable and intermittent snowpack. The highest flow rates are generated by rain-on-snow events during warmer days in winter ( $Q \approx 0.1 \text{ m}^3 \cdot \text{s}^{-1}$ ), which is also the period when the simulation underestimates the dynamics of observed flow recession, especially in early 2013. High discharge rates can also happen during events with large amount of rainfall (typically in fall), while in summer the Strengbach stream does not dry and a low baseflow is always sustained.

#### 4.2. ET Fluxes

Numerical simulations closely capture the seasonal magnitude and timing of ET fluxes inferred from the eddy covariance flux towers based in Naizin and Auradé watersheds. In Naizin, the ET simulated over grassland cells manages to reproduce the observed rising limb until the early summer (Figure 6a,  $R^2 = 0.58$ , peak at 3–4 mm/day), despite a slight model overestimation in late summer. The observed ET rates decreasing below 0.5 mm/day in the subsequent fall are also well captured. In Auradé, the ET simulated over wheat cells display an even more consistent agreement with measurements (Figure 6b,  $R^2 = 0.60$ ). Observed and simulated ET fluxes peak at 5 mm/day in late spring, reach a minimum value below 0.5 mm/day in winter, and shows a slower increase in early spring and a faster decrease in summer after harvest. The same evaluation of the simulated ET is not possible for the Strengbach watershed as data from an eddy covariance flux tower were not available. Simulations however indicate lower mean ET ( $\approx 0\text{--}2 \text{ mm/day}$ ) except during precipitation events due to a much larger vegetation interception (up to  $\approx 4 \text{ mm/day}$ ).

#### 4.3. Piezometric Levels

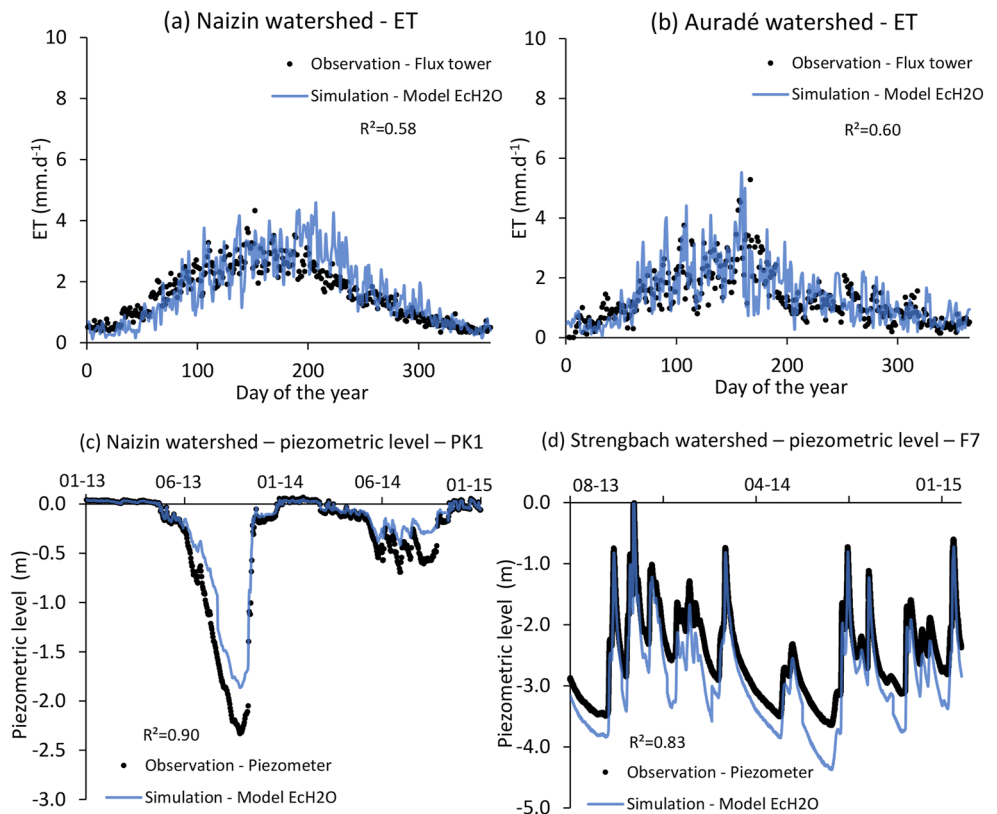
We also compared the water levels measured in several piezometers located along slopes with the depth of aquifers simulated by EcH<sub>2</sub>O-iso along the 2013–2014 time period, and we here report two examples in Naizin and Strengbach (Figures 6c and 6d). In Naizin, relatively simple and large seasonal variations are observed for piezometric levels. In the piezometer PK1 located near the valley bottom and within the hydromorphic zone, the water level is close to the soil surface in winter ( $z \approx 0 \text{ m}$ ) and spring ( $z \approx -0.1 \text{ m}$ ), but notably decreases during a long period in summer and fall (down to  $z \approx -2.2 \text{ m}$ , Figure 6c,  $R^2 = 0.90$ ). Groundwater fluctuations are along shorter time scales in the Strengbach where piezometric levels can fluctuate between each significant precipitation events (Figure 6d,  $R^2 = 0.83$ ). For example, in the borehole F7 located along slopes in the northern part of the watershed, the water level rapidly increases toward the soil surface and decreases down to 2–3 m depth within few weeks. The same evaluation of the simulated aquifer depths is not possible for the Auradé watershed as piezometers were not monitored over the study period.

### 5. Results and Model-Based Insights Into Watershed Functioning

The ability of the integrated modeling to capture such variety of observations gives confidence to analyze the differences of hydrological functioning between these three contrasting watersheds. In the following, we exploit the modeling results to highlight the contrasts of water partitioning, water transit times, and water storage dynamics.

#### 5.1. Difference of Hydrological Partitioning

A first analysis can be made from the simulated partition of hydrological fluxes associated with the main processes controlling the water cycle (i.e., stream water discharge at the outlet, evaporation of soil water, evaporation of intercepted water, and transpiration; Figure 7).

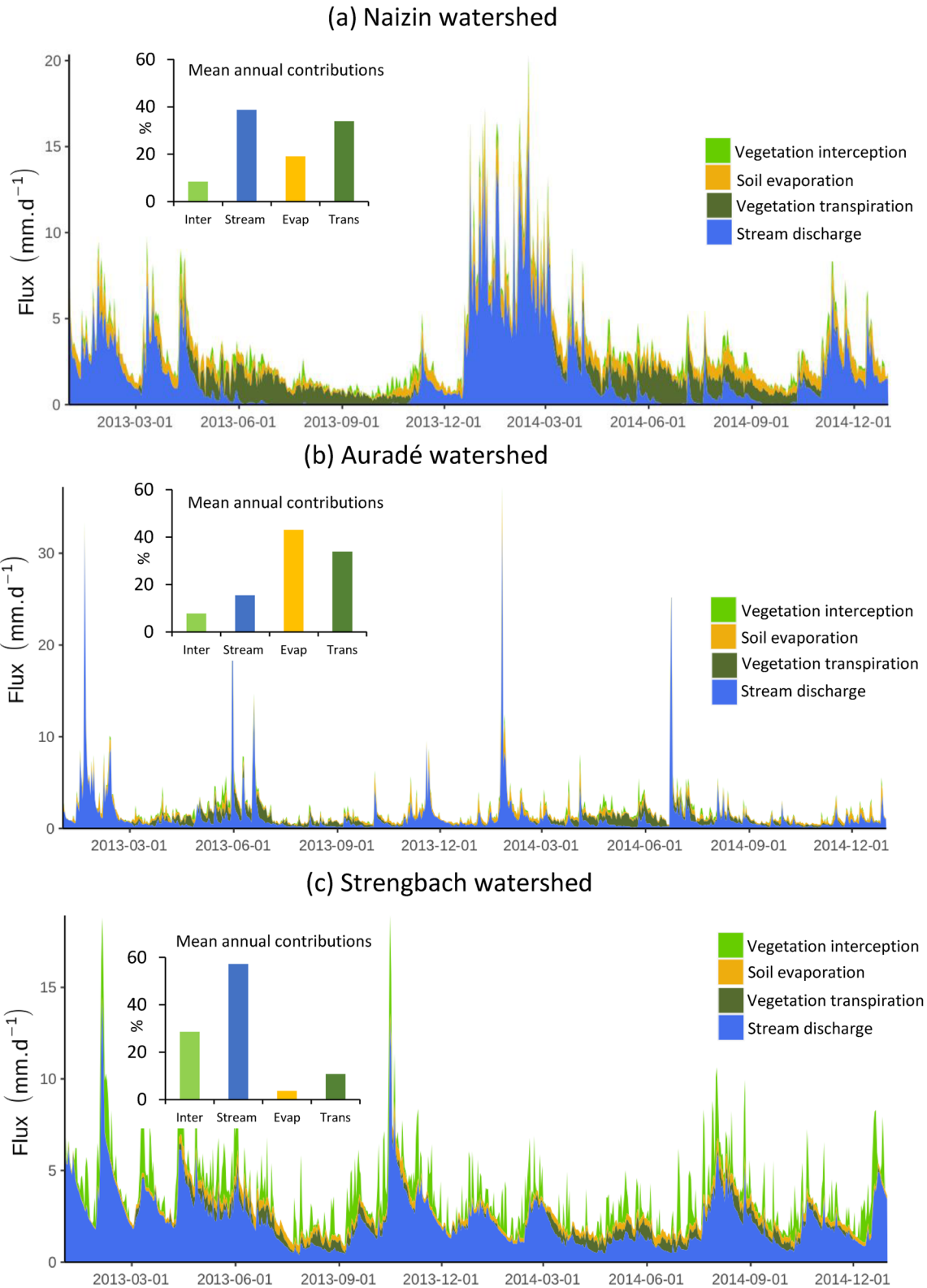


**Figure 6.** Seasonal cycle of daily scale evapotranspiration (ET) fluxes in Naizin and Auradé (a–b) and water table levels in Naizin and Strengbach (c–d). Black dots show observations and blue lines display simulations. In Naizin, panel (a) compares the simulated ET averaged between 2013 and 2014 to averaged eddy-covariance measurements in 2016–2017 over a grassland area (see Section 3.2), while panel (c) compares modeled and observed water table fluctuations in 2013 at piezometer PK1 in the riparian area. In Auradé, panel (b) compares simulated and observed ET fluxes for year 2013 over a wheat-sown area. In the Strengbach, panel (d) shows model-data comparison of groundwater levels at the hillslope borehole F7 from August 2013 to December 2014.

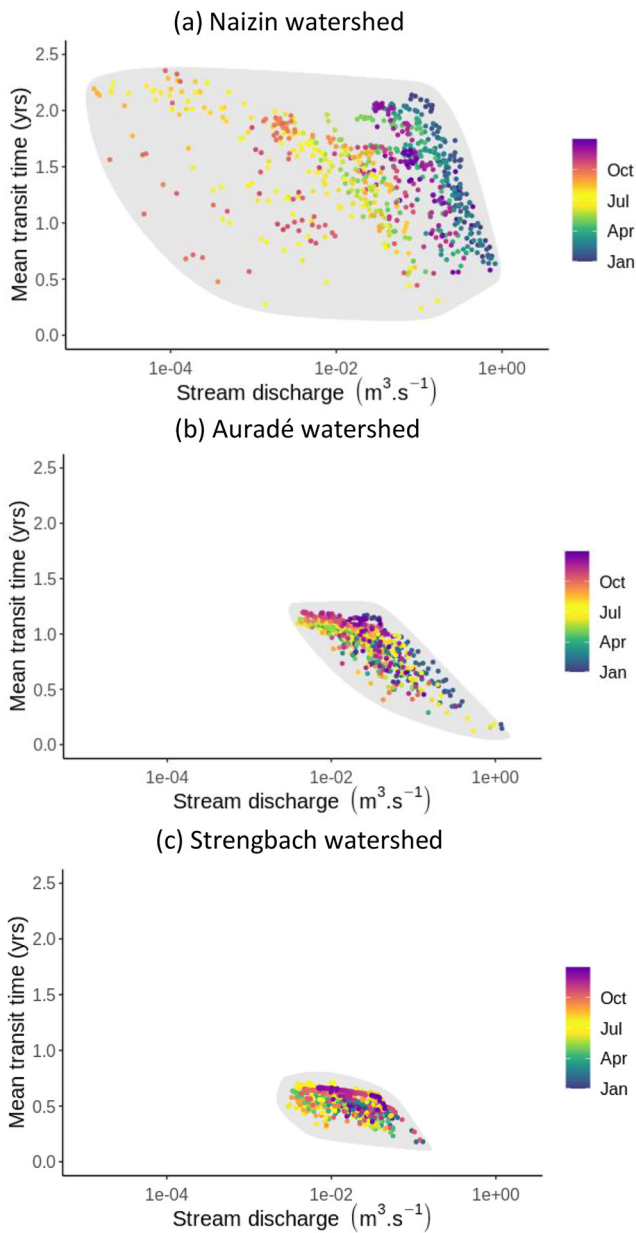
In the Naizin watershed, the simulated partition of hydrological fluxes shows a simple seasonality, with a water budget dominated by stream discharge in winter and ET in summer (Figure 7a). ET fluxes are dominated by vegetation transpiration when the vegetation is active in summer. In winter, when the vegetation is less active, the ET is much lower in general and is more dominated by the soil evaporation. The vegetation interception is never a dominant process due to the limited interception capacity of wheat and maize crops (Figure 7a).

Such a strong seasonality of water partitioning is not found in Auradé, where ET processes dominate at the watershed scale for most of the year (Figure 7b). Due to the presence of bare soils in some fields before the growing season of sunflowers and the frequent occurrence of hot temperatures, the soil evaporation is an important process in the total ET. Only two situations arise where stream water fluxes are dominant: a short period in winter characterized by frequent rainfall events and higher average stream water discharge rates during a few weeks, and brief events (hourly to daily scales) associated with intense thunderstorms and resulting high stormflow at the outlet (Figure 7b).

The Strengbach watershed is characterized by the year-round predominance of stream water fluxes (Figure 7c). Only in the summer do ET fluxes outpace water outputs at the catchment scale, noting that this summer period is shorter than in the other studied watersheds. Another specificity of this watershed is that evaporation of vegetation interception is the main ET component across seasons. Contrary to agricultural watersheds, the dense forest cover can efficiently intercept precipitation, even in winter, due to the presence of evergreen spruce trees in a large part of the watershed. Comparatively, the vegetation transpiration is lower due to the fact that a frequently wet vegetation transpires less, but also due to the more energy-limited and much colder settings in this mountainous watershed (Table 1).



**Figure 7.** Partition of hydrological fluxes simulated by the ecohydrological model ECH<sub>2</sub>O-iso in the three watersheds for years 2013–2014. The partition is shown as stacked hydrological fluxes at hourly resolution with the light green used for the fluxes associated with the vegetation interception, the yellow used for the soil evaporation, the dark green used for the vegetation transpiration and the blue used for the stream discharge. Subplots (a–c) show results for the Naizin, Auradé, and Strengbach watersheds, respectively. Insets provide the relative contribution from each process at a multiyear timescale (2007–2014).



**Figure 8.** Mean transit times of stream water versus stream water discharges at the outlet of the three watersheds for years 2013–2014. Each point represents one daily averaged water transit time and water discharge calculated by the model  $ECH_2O$ -iso. The color scale highlights the period of the year to better visualize the seasonal patterns emerging from the modeling results. Blue color is used for the winter, green for the spring, yellow for the summer, and purple for the fall. Gray envelopes were drawn around the cloud of points to additionally highlight the general trends of water transit times. Subplots (a–c) show results for the Naizin, Auradé, and Strengbach watersheds, respectively. Scales are identical to highlight variations between watersheds.

brief (Figure 9a). This strong seasonality, which is one particularity of Naizin, is also visible in the annual trajectory of water storages. In terms of relative variations,  $S$  increases by approximately 6% during the wettest periods from the reference value on 1 October ( $S_{\text{normalized}} \approx 1.06$  in winter) and decreases by around 3% in the driest conditions in early fall ( $S_{\text{normalized}} \approx 0.97$  in early fall; analysis shown for the hydrological year 2012–2013; Figure 10a). In Naizin, under observed climatic conditions and given its CZ characteristics, the important total

### 5.2. Difference of Water Transit Times

$ECH_2O$ -iso also allows to estimate the mean transit times (MTTs) of water in several CZ compartments and their variability throughout the year. Across the three watersheds, the longest MTTs of stream water are simulated in the Naizin watershed, ranging between 0.5 and 2.5 years (Figure 8a). While a marked seasonality is apparent with older most often found during summer low-flow conditions, the stream MTT relationship with discharge shows a wide distribution implying that waters with relatively long transit times can be found in the stream through the year and over a wide range of hydrological conditions. The simulated MTTs in the underlying groundwater aquifer are comparatively longer (1.3–2.7 years), while transpiration MTT in vegetation transpiration (0.2–1 years) and soil evaporation (0.9–2.1 years) are shorter (Figure S1).

Shorter stream water MTTs are found in the Auradé watershed (Figure 8b). Stream water MTTs vary between 0.1 and 1.3 years with a narrower, inverse relationship with discharge implying that waters with long transit times are simulated during low flow periods while short transit times are exclusively found during flood events. The distribution shows a weak seasonality, especially for intermediate and long MTTs that can occur at any season. In comparison with stream waters, simulated MTTs in groundwater at Auradé are longer (2–3.5 years) and even surpass the groundwater ages found in Naizin, while water MTT associated with vegetation transpiration (0.4–1 years) and soil evaporation (0.1–1.1 years) are shorter than those found in stream water (Figure S1).

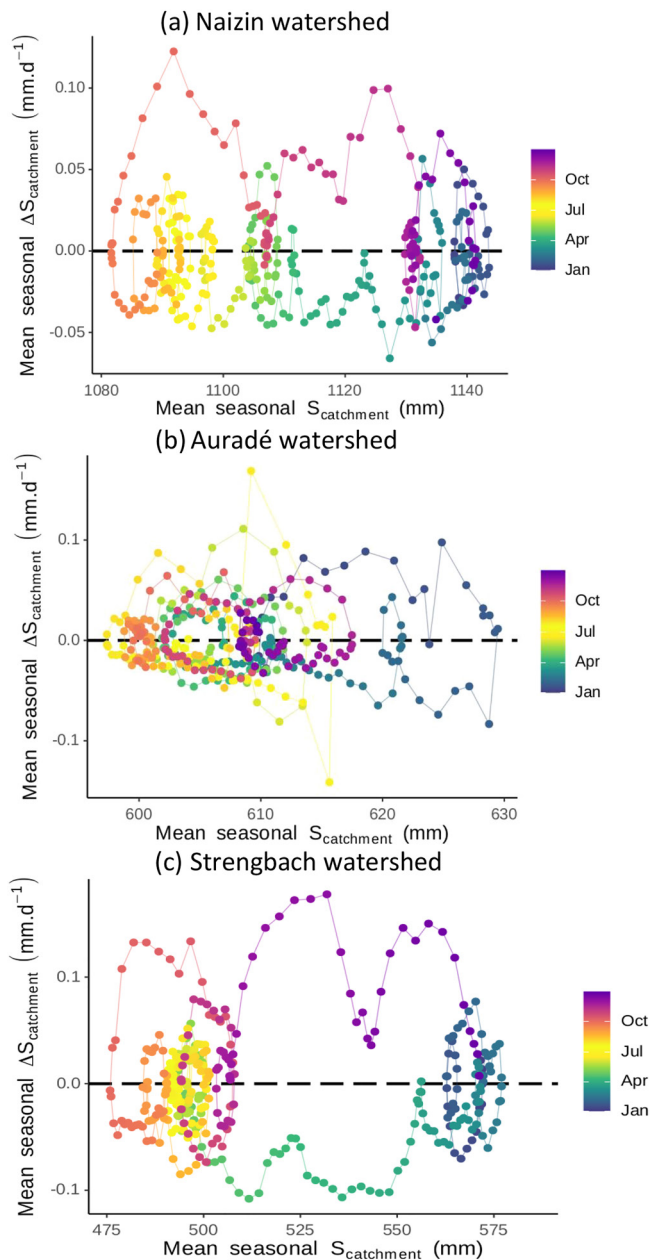
The shortest stream water MTT is simulated in the Strengbach (Figure 8c), ranging from a few weeks to a few months (0.1–0.7 years). As in Auradé, the distribution against stream discharge is inverse, but relatively wide: that waters with short transit times are only simulated during high flow periods but intermediate MTTs are found over a wider range of water discharges. Some degree of seasonality is apparent, with the highest MTTs simulated in summer and the lowest during winter or fall floods, yet intermediate MTT can occur at any season. In comparison with stream waters, simulated MTT for aquifer waters are slightly longer (0.3–0.8 years) but much shorter than at the two other watersheds, as are the MTTs of vegetation transpiration (0.1–0.3 years) and soil evaporation (0.1–0.7 years; Figure S1).

### 5.3. Difference of Total Water Storage Dynamics

One of the other major interest of this integrated modeling is also the opportunity to study the CZ water storage and its variability (Section 3.4). These hydrological characteristics can only be estimated by modeling approaches.

We find first that the Naizin watershed is characterized by the highest simulated total storage ( $S \approx 1,080$ – $1,150$  mm, expressed in water height equivalent), with a minimal  $S$  reached in early fall and a maximal  $S$  reached in winter (Figure 9a). Recharge periods with positive storage variations ( $\Delta S$ ) and increasing  $S$  mainly occur in fall and early winter while the storage decrease periods span over spring and summer. The trajectory in the  $S$ - $\Delta S$  phase space also indicates that this catchment stations a long time in a high-storage state in winter, while the time spent around the minimal  $S$  is





**Figure 9.** Dynamics of the total water storage ( $S$ ) calculated by the model EcH<sub>2</sub>O-iso in the three watersheds. Calculation was performed for multiyear daily averages from 2007 to 2014 to extract the general behavior at a decadal timescale in each watershed. The  $x$  axis shows the total water storage expressed as a water height in mm while the  $y$  axis represents the daily averaged variation of the total water storage in  $\text{mm}\cdot\text{day}^{-1}$ . Each point represents one multiyear daily average. The color scale highlights the period of the year to better visualize the seasonal patterns emerging from the modeling results. Blue color is used for the winter, green for the spring, yellow for the summer, and purple for the fall. Subplots (a–c) show results for Naizin, Auradé, and Strengbach watersheds, respectively. Scales were adapted for each watershed to highlight respective seasonal dynamics.

water storage ( $S \approx 1,080\text{--}1,150$  mm) varies by less than 9% during a typical hydrological year.

Simulated total storage is lower for the Auradé watershed ( $S \approx 590\text{--}630$  mm), with a minimal  $S$  reached in late summer and a maximal  $S$  reached in winter (Figure 9b). Strong recharge events with high positive  $\Delta S$  are characteristic of the early summer (thunderstorm period), but these events are quickly mirrored with discharge days (negative  $\Delta S$ ). The effective recharge period with consistently positive  $\Delta S$  and increasing  $S$  only occurs in a part of the winter (January–February). A significant discharge with negative  $\Delta S$  and decreasing  $S$  happens in late winter, and can be further seen in spring and summer. The trajectory in the  $S$ - $\Delta S$  phase space also implies that the period with important storage is brief in winter while the duration spent with low storage is much longer for Auradé (Figure 9b). These water storage dynamics reflect the more transient hydrological functioning of Auradé. The normalized phase space diagram for storage shows that compared its values on 1 October,  $S$  increases by approximately 7% during the wettest periods ( $S_{\text{normalized}} \approx 1.07$  in winter) and decreases by around 3% in the driest conditions ( $S_{\text{normalized}} \approx 0.97$  in late summer; analysis shown for the hydrological year 2012–2013; Figure 10b). The moderate total water storage ( $S \approx 590\text{--}630$  mm) therefore varies by less than 10% during a typical hydrological year.

The Strengbach is characterized by the lowest total storage across the studied watersheds ( $S \approx 475\text{--}575$  mm, Figure 9c). The minimum  $S$  value is reached in early fall, while the yearly maximum storage occurs in winter. Recharge periods with positive  $\Delta S$  and increasing  $S$  are clearly distinguishable in fall and early winter while a marked discharge period mainly spans the springtime. In between, the hydrological trajectory of this watershed remains several weeks in winter in a high-storage state, while an even longer low-storage state is apparent in summer with a minimal storage state in early fall. This highly seasonal trajectory of the storage states in the Strengbach watershed is closer to Naizin than it is to Auradé. In relative terms,  $S$  increases by approximately 25% during the wettest periods ( $S_{\text{normalized}} \approx 1.25$  in winter) and decreases by around 7% in the driest conditions ( $S_{\text{normalized}} \approx 0.93$  in early fall; analysis shown for the hydrological year 2012–2013; Figure 10c). The limited CZ water storage ( $S \approx 475\text{--}575$  mm) in the Strengbach changes by more than 32% during a typical hydrological year, which is the largest relative variation of the three watersheds.

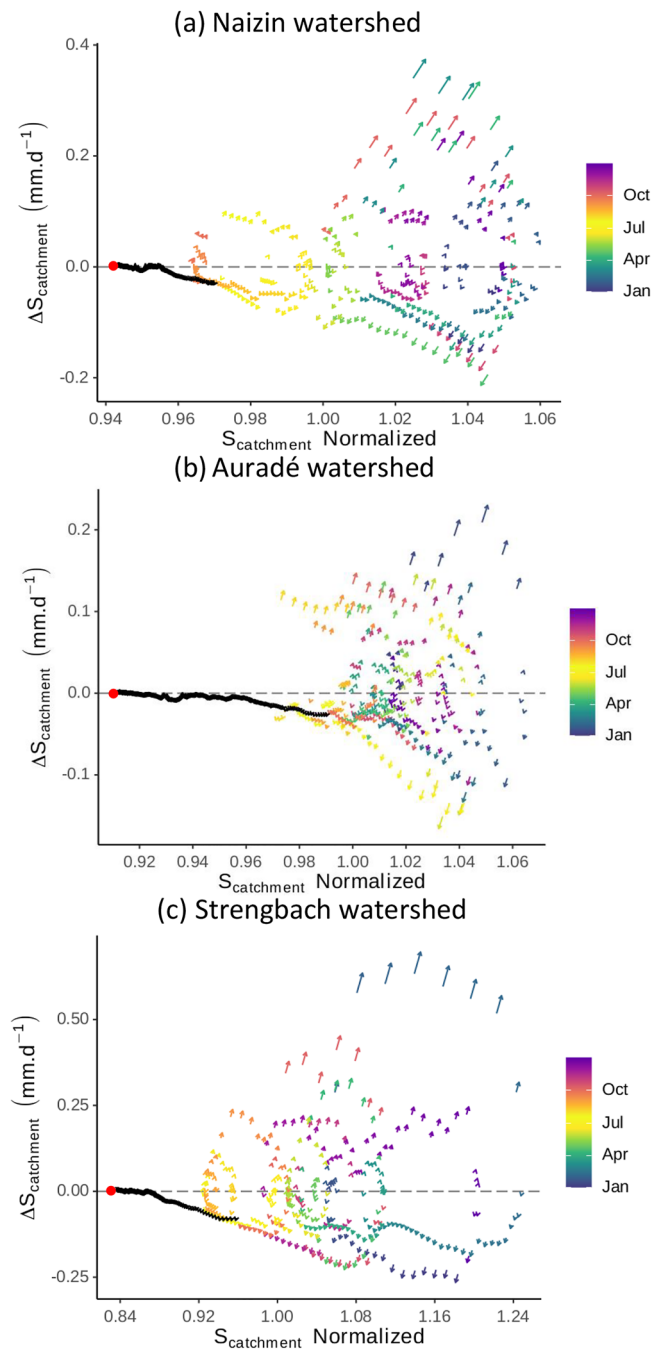
#### 5.4. Difference of Active and Inactive Water Storage Components

We extended the analysis of storage dynamics through quantifying the hydrologically active fraction of  $S$  in each watershed with virtual dry-out experiments (Section 3.4), mapped with the black symbols (drying trajectory) and the red dots (no-flux state) in Figure 10. In Naizin, simulations of drying trajectories when precipitation is set to zero indicate that nearly 94% of CZ storage is hydrologically inactive ( $S_i$ ), while only 6% is hydrologically active. Drying trajectories in Auradé yield values of about 91% for hydrologically inactive storage, with 9% of active storage. In the Strengbach, we find that up to 18% of  $S$  belongs to the hydrologically active water storage ( $S_a$ ), while 82% is inactive.

## 6. Discussion

### 6.1. Uncertainties and Model Limitations

While the ecohydrological simulations capture most of the characteristics displayed by the evaluation data sets, mismatches also allow to discuss



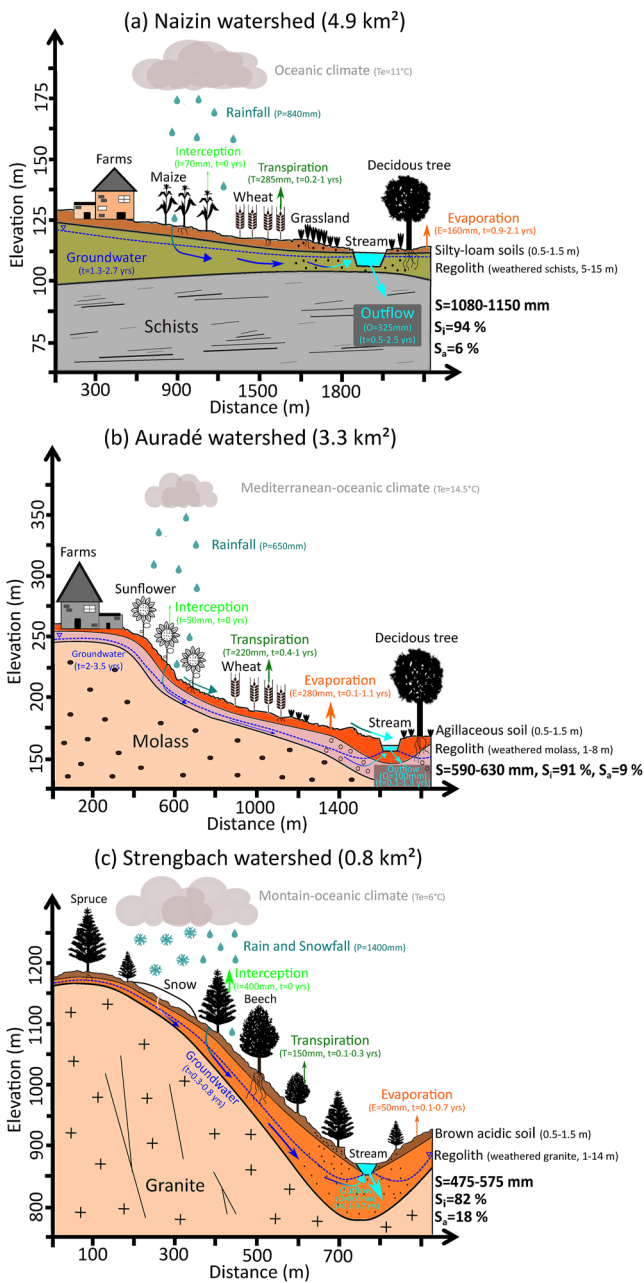
**Figure 10.** Vector fields representing the dynamic of the total water storage calculated by the model  $\text{EcH}_2\text{O-iso}$  in the three watersheds. The  $x$  axis shows the total water storage normalized to the storage at the beginning of the hydrological year while the  $y$  axis represents the daily averaged variation of the total water storage in  $\text{mm}\cdot\text{day}^{-1}$ . Rising arrows indicate a day of storage increase while falling arrows show a day of storage decrease. Colored arrows display results for the hydrological year 2012–2013 under observed atmospheric forcing and unchanged precipitation. The color scale highlights the period of the year to better visualize the seasonal patterns emerging from the modeling results. Blue color is used for the winter, green for the spring, yellow for the summer, and purple for the fall. Black trajectories display results of drying trajectories obtained from simulations over the hydrological year 2013–2014 when precipitation is set to zero at the beginning of this hydrological year and over this whole year. Red dots represent the no-flux state of each watershed and mark the separation between active and inactive total water storages. Subplots (a–c) show results for Naizin, Auradé, and Strengbach watersheds, respectively.

current model limitations and uncertainties. The overestimation of stream water outflow during some important floods of the wet winter 2013–2014 in Naizin (Figure 5a) may reflect the limitation of the simple conceptualization of the subsurface-channel seepage flux. Conversely, the underprediction of few flash floods in Auradé during major thunderstorms (Figure 5b) may highlight the limits of simplified stream networks with constant channel geometry during such high-intensity events. In the Strengbach watershed, the stream water discharges are clearly better simulated when snow is absent compared to periods with a thick snowpack (Figure 5c). It may point at the need for improving the dynamics of the currently simplified snowpack module to account for rain-on-snow interactions, but also for adding the effect of intercepted snow spill-over currently neglected in the model's formulation.

Water transit times determined by  $\text{Ech}_2\text{O}$ -iso can be compared with independent estimations of stream and aquifer water MTTs obtained from geochemical analysis and other modeling studies. In Naizin, the dating based on chlorofluorocarbon tracers (CFCs) indicates groundwater MTTs between 1.2 and 12 years, depending on the choice of the porosity used in calculations (Molénat et al., 2013). Using a high value of porosity ( $\approx 40\%$ ) for groundwater flows has led to the higher MTTs ( $\approx 12$  years), while using a lower porosity (10%–20%) gave shorter MTTs ( $\approx 1.2$ –2.4 years; Molénat et al., 2013). A porosity of 40% is possible in soils, but seems too high for a weathered regolith at few meters of depth (Ackerer et al., 2020), and a previous study involving a spatially distributed hydrological modeling also proposed a porosity of approximately 20% in the aquifer of Naizin (Gascuel-Oudoux et al., 2010). Such effect of the porosity choice on water transit times has been recently discussed by Marçais et al. (2022). The simulated stream and groundwater MTTs determined by  $\text{Ech}_2\text{O}$ -iso and using a calibrated porosity in the range of 25%–12% are therefore in accordance with the lower range of MTTs inferred from CFCs in Naizin. Several independent estimations of stream and aquifer water MTTs were gathered from several previous studies in the Strengbach. Hydrological simulations performed with the physically based model NIHM yielded stream water MTTs of approximately 0.2–0.6 years (Weill et al., 2019), very similar to the range we found (0.1–0.7 years). Reactive-transport simulations were also conducted to model concentration-discharge relationships of several solutes in the Strengbach watershed, reporting spring water MTTs of 2–4 months from these geochemical constraints (Ackerer et al., 2020). Other water age estimates in deep boreholes derived with an exponential mixing model with CFC data have suggested much older waters beyond 25 m depth (30–150 years; Ranchoux et al., 2021).

It is however important to underline that the oldest and deepest waters found in the fractured bedrock of the Strengbach watershed are characterized by slow velocities and have a very limited contribution to overall water fluxes at the watershed scale (notably compared to shallow subsurface fluxes; Ackerer et al., 2021). Because  $\text{Ech}_2\text{O}$ -iso was calibrated to reproduce the major components of the contemporary water cycle (stream outflows, total ET), the deepest and oldest waters are unlikely to be included in the simulated MTTs, precisely because they represent a minor part of the overall water budget. We acknowledge that  $\text{Ech}_2\text{O}$ -iso's simulations potentially miss the oldest waters stored in the fractured bedrocks, although it is very likely that we encompass the majority of the water fluxes in the three watersheds. In Auradé, we here provide the first MTTs quantification to date, further studies will be needed for independent comparisons.

The total water storages used in simulations can also be compared with additional estimations. In Naizin, an approximate calculation using the mean regolith thickness observed by SRT ( $\approx 7$  m) and the regolith porosity used by an independent modeling study ( $\approx 20\%$ ; Gascuel-Oudoux et al., 2010) leads to a subsurface water storage of about 1,400 mm. As the seismic refraction profile does not include the hydromorphic zone where soils and regolith are thinner, the average subsurface storage at the watershed scale is probably lower than 1,400 mm, and  $\text{Ech}_2\text{O}$ -iso's estimate of CZ storage (1,080–1,150 mm) seems reasonable. In Auradé, a similar first-order calculation considering mean regolith thickness from SRT ( $\approx 5$  m) with a porosity determined by an independent modeling study ( $\approx 10\%$ ; Ferrant et al., 2016) leads to a subsurface water storage of about 500 mm. Although this evaluation is approximate,  $\text{Ech}_2\text{O}$ -iso's estimates of the total water storage ( $S \approx 590$ –630 mm) are within this order of magnitude. A more precise estimation of the water volume stored in the subsurface of the Strengbach watershed can be obtained from recent geophysical investigations involving magnetic resonance sounding (Lesparre et al., 2020). Expressed in equivalent water height, subsurface water storage during wet conditions varies from 200 to 500 mm (in April 2013), with lower subsurface storage values along crests where the regolith is thinner and higher values in the valley bottom where the regolith is much thicker. These estimates are in the same order of the values reported in this modeling study (475–575 mm), with differences that can be explained by the spatial and temporal variability of storage but also by the fact that  $\text{Ech}_2\text{O}$ -iso's CZ storage includes aboveground



**Figure 11.** Summary figure highlighting the critical zone (CZ) heterogeneity and the major modeling results obtained from this multi-observatory study. The schematic representation of the CZ heterogeneity includes the differences of geological history, of geomorphology, and of soil and regolith types and thicknesses. Vertical scales for soil and regolith thicknesses were exaggerated for visibility purpose. The main characteristics of land use and vegetation type are also represented. Mean annual water fluxes and mean water transit times calculated by the model  $\text{EcH}_2\text{O-iso}$  are shown for the major hydrological processes controlling the water cycle. Total water storage ( $S$ ) and fractions of active ( $S_a$ ) and inactive ( $S_i$ ) total water storage inferred from simulations are also given. Subplots (a–c) provide the summary overview for the Naizin, Auradé, and Strengbach watersheds, respectively.

compartments too (ponding, snowpack), and not only the subsurface storage. In addition, the relative variation of  $S$  inferred from our study (32%) is similar to the annual storage amplitudes suggested by the physically based model NIHM in the Strengbach (variations of 20%–30%; in Weill et al., 2019).

The comparison of water transit times suggested that the deepest and oldest waters are not captured by simulations, as the  $\text{EcH}_2\text{O-iso}$  model setup for this study does not include the CZ compartment corresponding to deep and fractured bedrock. However, the weathered and porous regolith has been shown to contain much more water than the fractured bedrock (Ackerer et al., 2021), and our storage estimate may only slightly underestimate the exact CZ water storage. In addition, adding this deeper water compartment may only contribute to the inactive water storage in watersheds, as deep waters stored in the fractured bedrock have no clear connection with the hydrological network, at least in the Strengbach watershed (Ackerer et al., 2021). To summarize, our CZ water storage estimates are therefore consistent with the independent information at hand, but additional geophysical profiles would be helpful to refine estimates and model evaluation, especially for the regolith thickness inferred in Naizin and Auradé watersheds.

## 6.2. The Hydrological Diversity Between the Three Contrasted Watersheds

The comparative dimension of this study opens the opportunity to evaluate the differences of hydrological functioning across three contrasted regions, as summarized in Figure 11. A first-order difference comes from the repartition of the overall water loss. ET processes represent approximately 60% of water output in Naizin, up to 80% in Auradé, but only 40% in the Strengbach (Figure 7). In Naizin, the simulated multiyear average fluxes indicate that the average rainfall of 840 mm is partitioned between approximately 325 mm of stream water discharge, 160 mm of soil evaporation, 285 mm of vegetation transpiration, and 70 mm of vegetation interception (Figures 7a and 11a). Such hydrological partitioning implying a moderate dominance of ET over runoff is also reported by field observations (Fovet et al., 2018). The simulated multiyear average fluxes indicate that the average rainfall of 650 mm is partitioned between approximately 100 mm of stream water discharge, 280 mm of soil evaporation, 220 mm of vegetation transpiration, and 50 mm of vegetation interception in Auradé (Figures 7b and 11b). The major role of ET in the hydrological budget of this site is consistent with field-based studies (Béziat et al., 2013; Tallec et al., 2013). For the Strengbach, the simulated multiyear average fluxes indicate that the average rainfall of 1,400 mm is partitioned between approximately 800 mm of stream water discharge, 50 mm of soil evaporation, 150 mm of vegetation transpiration and 400 mm of vegetation interception (Figures 7c and 11c). The role of vegetation interception in the ET component was also independently documented by interception and sap flow measurements (Viville et al., 1993), while the dominance of stream outflow at the watershed scale was investigated by hydroclimatic budgets (Cotel et al., 2020; Pierret et al., 2018).

Hydrological diversity also exists for water pathways and especially for the unequal repartition of water fluxes along the CZ vertical layers. In Naizin,  $\text{EcH}_2\text{O-iso}$  simulations indicate that surface runoff is relatively rare (1–2 events per year) with well-drained silty loam soils in most of the watershed, and occurs only during summer thunderstorms or winter storms. Subsurface flow paths are dominant and may be deep along slopes



and nearby hill crests (0–10 m), contrasting with valley bottoms where hydromorphic soils are present and regolith is thinner (0–3 m). Surface runoff is much more frequent in Auradé, occurring during high-intensity precipitation due to a combination of factors including clay-rich and low-permeability soils, agricultural plots with bare soils, and tilled hilly slopes. Among the three watersheds, Auradé is the one with the least important subsurface water fluxes (Figure 11b). By contrast, there is almost no surface runoff simulated in the Strengbach due to well-drained and porous brown soils. There, subsurface flows are largely dominant, both occurring in the soil (0–1 m) and in the regolith while remaining relatively shallow (1–5 m of deep along slopes, Figure 11c).

Differences of hydrological functioning are also visible for subsurface-channel interactions. In Naizin, the channel interacts with the subsurface water along the hydromorphic zone. These exchanges are however intermittent, as the channel gets disconnected from the subsurface water during dry periods. In Auradé, the transfer of water from the subsurface to the channel preferentially occurs at the bottom of hilly slopes where the higher conductivity of the colluvial deposits enhances water exchanges. Even if the subsurface fluxes are less important at the annual scale for Auradé, a slow but sustained water flow exists from the subsurface to the channel during most of the year. In the Strengbach, subsurface-channel interactions are important along the saturated zone, and EcH<sub>2</sub>O-iso's simulations indicate that the water transfer from the subsurface to the stream is active year-round.

### 6.3. Stream Persistence and Interactions With Land Use and Climate Characteristics

Although Naizin has the largest total water storage (Figure 9a), the stream in Naizin is the most intermittent among the three watersheds and shows frequent summer periods with zero flow (Figure 5a). This feature is partially explained by the channel-subsurface disconnection occurring in summer and by the large fraction of inactive water storage in the watershed (Figure 10a), implying that the stream can dry up while substantial inactive groundwater storage is still present in the regolith. But the hydrological functioning and the stream persistence depend both on watershed internal properties and external forcings such as climate characteristics and land use changes. The oceanic climate in Naizin is characterized by frequent and low-intensity precipitation in winter and by drier atmospheric conditions in summer. Combined to well-drained soils, these settings attenuate surface runoff and promote an efficient groundwater recharge in winter. By opposition in summer, the moderate precipitation and the high ET of agricultural crops (3–4 mm/day) limit the recharge of the subsurface water storage. The most important anthropogenic impact in this watershed is the effect of intensive agriculture (Fovet et al., 2018), and agricultural activities exert a strong pressure on land use and have led to cereal crops that are known for their high water demand in summer. This crop ET acts in concert with the small fraction of active water storage, leaving little to sustain stream flow in summer. The large fraction of inactive storage also explains the longer stream MTTs found in Naizin, due to the model simplified conceptualization for the tracking of water signatures (e.g., water ages): subsurface compartments are well-mixed without explicitly distinguishing active (young) and inactive (old) storage components, especially in the regolith layer where subsurface seepage to the stream can occur, so that the age of groundwater-fed baseflow carries part of the signature of inactive storage. These interactions between internal and external characteristics also explain the strong seasonality of the total water storage, with a long period of high total storage in winter, a relatively long period of low storage in summer, and clear transitional patterns in spring and fall (Figure 9a).

For Auradé, the stream flows during most of the year, although low flow is observed during long periods and that the stream can dry up in fall during dry years. On the one hand, the climate characterized by hot summer temperatures, heterogeneous precipitation, and high ET of agricultural crops explains the long extent of the low discharge periods in Auradé. On the other hand, the higher fraction of hydrologically active storage in Auradé (Figure 10b) implies that the stream has a more sustained based flow compared to Naizin. Similarly to Naizin, the major anthropogenic impacts on the water cycle are also associated to intensive agriculture in this watershed (Ferrant et al., 2016; Ponnou-Delaffon et al., 2020). Agricultural practices have led to the presence of sunflower crops covering roughly one-third of the watershed (Figure 3f) and characterized by a late growing season in the early summer (Taghavi et al., 2010). This crop choice results in having bare plots with low-permeability, clay-rich soils along moderate-to-steep hillslopes during the thunderstorm season in late spring, favoring fast surface runoff pathways. In interaction with the atmospheric forcing, an accentuation of the transient behavior of the water cycle is then promoted by the agricultural practices in the Auradé watershed (Figure 11b). Such transient hydrological functioning is also visible on the chaotic dynamics of the total water storage. A brief period of high

total water storage exists in winter, while a long period of low storage with an absence of clear seasonal patterns occurs the rest of the year with only sporadic recharge during thunderstorms (Figure 9b).

In the Strengbach, the stream is perennial and sustained by water flow from the saturated zone, which is itself subsidized by lateral subsurface flow along the hillslopes. Although the Strengbach has the smallest total water storage (Figure 9c), it also displays the highest fraction of hydrologically active water storage to maintain stream flow (Figure 10c). But stream persistence is also influenced by climatic characteristics. One particularity of this watershed is the relative abundance and frequency of precipitation throughout the year, including important snowfall and rainfall events in winter and spring when ET outputs are low. These wet conditions imply faster subsurface water flow as hydraulic conductivities are often close to their value at saturation, favoring shorter water transit times. We can thus deduce that in the Strengbach, the stream is perennial not because the dynamic storage drains slowly, but because the watershed's subsurface is frequently and sufficiently refilled by new water (sustained turnover). Anthropogenic impacts are more limited in the Strengbach watershed and are restricted to forest management within a mountain landscape unaffected by agriculture or buildings (Cotel et al., 2020; Pierret et al., 2018). The absence of soil compaction from agricultural activities preserved the high infiltration capacity of sandy soils, in turn favoring groundwater recharge and stream baseflow. The wet and much colder mountain climate also tends to limit ET processes, and even with an important canopy interception, the precipitation are sufficiently abundant to subsidize the active water storage (Figure 11c). The seasonal dynamics of the total water storage reflect the hydrologically functioning of the watershed, with a high water storage in winter and early spring during snowmelt period, a low storage in early fall, and clear transition phases in spring and fall (Figure 9c).

#### 6.4. Long-Term Evolution, CZ Heterogeneity, and Modulation of the Water Cycle

This study offers a rare opportunity to explore how different pathways of long-term evolution generate CZ heterogeneity and how they promote a diversity of hydrological functioning in interactions with regional climates and more recent anthropogenic impacts (summary Figure 11).

The Brioverian schists found in the Naizin watershed (age  $\approx$  550 Myr) have undergone multiple phases of weathering since their formation with a likely major weathering phase during the first half of the Tertiary (Wyns et al., 2004). During the Quaternary, the watershed's geomorphological evolution was marked by a fluvial incision of the unconsolidated weathered material (i.e., the regolith), shaping its current variability with a thinner regolith near the stream network ( $\approx$ 3–4 m) and thicker regolith on hilltops ( $\approx$ 10–15 m, Figure 11a). A relatively deep aquifer developed in the thick weathered material (Gascuel-Oudoux et al., 2010), which explains several hydrologic features including the high total water storage ( $S \approx$  1,080–1,150 mm) and the longer stream water MTT in Naizin (0.5–2.5 years) compared to the other studied watersheds. In addition, the absence of a significant tectonic uplift in the Brittany region for several million years resulted in a relatively flat landscape in Naizin (0%–5%, Guillocheau et al., 2003). This geomorphology limits gravity-driven drainage which also decreases the connectivity between the aquifer and the stream network. These considerations explain why Naizin, the flattest of the three watersheds (Figure 11a), also displays the largest fraction of inactive water storage ( $S_i$  of 94%) and a non-persistent stream. Finally, the weathering of schists has led to silty loam soils that are well drained in a large part of the watershed. Combined with climatic characteristics, this feature explains why the watershed is not prone to large surface runoff events and why the stream flow is mainly sustained by groundwater with longer transit times (Figure 11a).

In Auradé, the Miocene molasse (age  $\approx$  20 Myr) results from the erosion of the Pyrenees Mountains and the deposition of detrital materials in the Gascogne sedimentary fan (Perrin et al., 2008; Taghavi et al., 2010). The molasse was not deeply weathered but the Quaternary geomorphological evolution of the watershed was marked by solifluction processes and transport of colluvium along slopes (Taillefer, 1968). The current heterogeneity in the thickness of the weathered material reflects this evolution, with a thin regolith on steep slopes ( $\approx$ 2–3 m), moderate regolith thickness on flat hilltops ( $\approx$ 3–4 m), and thicker regolith downslope ( $\approx$ 5–8 m) where colluvial deposits are present in the zone bordering the stream network (Figure 11b). The thin aquifer developed in the weathered molasse with greater water storage downslope compared to hilltops controls several hydrologic features such as the moderate total water storage ( $S \approx$  590–630 mm) and the shorter water MTTs in Auradé (stream MTT  $\approx$  0.1–1.3 years). The hilly landscape and the steeper slopes found in Auradé also tend to enhance hydrological drainage and gravity-driven flows, which is one of the reason why the fraction of active water

storage is higher compared to Naizin ( $S_i \approx 91\%$ , Figure 11b). Such a landscape also favors stream flow persistence in dry periods through groundwater seepage at the bottom of hillslopes. Regarding the geochemical evolution, the chemical weathering of the molasse produced clay-rich soils that are naturally poorly permeable (Ferrant et al., 2014). This feature allows the occurrence of large surface runoff events in combination with the atmospheric forcing including high-intensity precipitation and the land use implying bare soils.

The Hercynian granite ( $\approx 315$  Myr) found in the Strengbach has undergone multiple phases of weathering since its formation (Chabaux et al., 2023), with the development of a deep pre-Triassic weathering profile (Lucas et al., 2017), similarly to other European Hercynian regions (Wyns et al., 2004). During the Quaternary, cold periglacial conditions and important erosion events reshaped the watershed and mobilized weathered material (Ackerer et al., 2022). Summits and crests were eroded while mobile regolith was stabilized at mid-slope and in the small valley bottoms, explaining the thin regolith currently found on crests ( $\approx 1$ – $2$  m) and the thicker regolith in the valley ( $\approx 8$ – $14$  m, Figure 11c). The thin aquifer developed in the weathered granite (Weill et al., 2019), except in a small area of the valley, influences several hydrologic features as the limited total water storage ( $S \approx 475$ – $575$  mm). The tectonic uplift associated to the Vosges Mountains formation and the Quaternary geomorphological evolution are responsible of the important relief and steep slopes found in the Strengbach (10%–45%; Ackerer et al., 2022; Ziegler & Dèzes, 2007). This geomorphology enhances hydrological drainage and gravity-driven flows, which in turn promote an efficient connectivity between the aquifer and the stream network. These considerations explain why the Strengbach, the steepest of the three watersheds (Figure 11c), also has the largest fraction of active water storage ( $S_a$  of 18%) and a perennial stream. Finally, the weathering of the granite has led to sandy brown acidic soils that are well drained in a large part of the watershed (Weill et al., 2019), excepted near the outlet in the saturated zone. This feature partially explains why the watershed is not prone to large surface runoff events. Combined with the steep slopes, sandy soils are also responsible of the fast subsurface water flow and the particularly short stream water MTTs in the Strengbach (0.1–0.7 years).

## 7. Conclusion

The large database from the three long-term observatories investigated in this study offers the opportunity to better depict the CZ heterogeneity and to understand how it generates different hydrological behaviors within contrasting territories (Figure 11). Ecohydrological simulations performed with the model EcH<sub>2</sub>O-iso and constrained by a wide range of observations crossing several disciplines show that a variety of processes operating at different timescales are interrelated in controlling the hydrological functioning of watersheds. The major outcomes from our comparative study can be summarized as follows:

- The long term CZ evolution controlling the regolith thickness strongly impacts the total water storage in watersheds.
- The Quaternary geomorphological evolution influences the current hydrological partitioning and the separation of hydrologically active and inactive water storage.
- Both internal watershed characteristics and external forcings, such as current atmospheric forcing and recent land use need to be considered to infer stream persistence and to understand hydrological diversity.
- The observed hydrological diversity cannot be fully understood without considering a continuum of time scales in CZ evolution.

Overall, this work illustrates the strength of CZ networks, allowing a new level of multi-site and comparative studies that are crossing several observatories and encompassing a wide diversity of geology and climate. Such an effort is key to acquiring a more detailed understanding of the current water cycle in watersheds, and will also play a crucial role in investigating future CZ trajectories. This is particularly true for apprehending the consequences of global changes in territories without ignoring the CZ heterogeneity and the diversity of hydrological functioning at regional scales.

## Data Availability Statement

All authors approved the final version of this article. Input data files and R scripts used for the post-treatment of EcH<sub>2</sub>O-iso simulations are available from the online Zenodo repository (Ackerer et al., 2023). The ecohydrological model EcH<sub>2</sub>O-iso is available from Kuppel et al., 2018b and additional information on model implementation can be found from Kuppel et al. (2020).

**Acknowledgments**

The study was conducted within the framework of WP2 (Data models—Interface) of the OZCAR Research Infrastructure (RI). OZCAR RI is funded by the French Ministry of Research, French research institutions, and universities. We also thanked the staff of the three CZ observatories for their long-term efforts of observation and data management (AgrHyS, OHGE, and Auradé observatories) and local stakeholders for their involvement and facilitation. Observation and research efforts in the three CZ observatories were financially supported by several institutes and contributors including CNRS (Centre National de la Recherche Scientifique), CNES (Centre National d'Etudes Spatiales), IRD (Institut de Recherche pour le Développement), INRAE (Institut National de Recherche pour l'Agriculture, l'alimentation et l'Environnement) and ANR (Agence Nationale de la Recherche). This work was also supported by Universities (University of Rennes, University Paul Sabatier of Toulouse, University of Strasbourg) and by the observatories of the INSU (Institut National des Sciences de l'Univers; OSUR, OMP, and EOST) and the INEE (Institut Ecologie et Environnement).

**References**

Ackerer, J., Jeannot, B., Delay, F., Weill, S., Lucas, Y., Fritz, B., et al. (2020). Crossing hydrological and geochemical modeling to understand the spatiotemporal variability of water chemistry in a headwater catchment (Strengbach, France). *Hydrology and Earth System Sciences*, 24(6), 3111–3133. <https://doi.org/10.5194/hess-24-3111-2020>

Ackerer, J., Kuppel, S., Braud, I., Pasquet, S., Fovet, O., Probst, A., et al. (2023). Exploring the critical zone heterogeneity and the hydrological diversity using an integrated ecohydrological model in three contrasted long-term observatories [Dataset]. *Water Resources Research*. Zenodo. <https://doi.org/10.5281/zenodo.10043984>

Ackerer, J., Ranchoux, C., Lucas, Y., Viville, D., Clément, A., Fritz, B., et al. (2021). Investigating the role of deep weathering in critical zone evolution by reactive transport modeling of the geochemical composition of deep fracture water. *Geochimica et Cosmochimica Acta*, 312, 257–278. <https://doi.org/10.1016/j.gca.2021.07.017>

Ackerer, J., Van der Woerd, J., Meriaux, A. S., Ranchoux, C., Schäfer, G., Delay, F., & Chabaux, F. (2022). Quantifying geomorphological evolution from <sup>10</sup>Be denudation rates: Insights from high-resolution depth profiles, topsoils, and stream sediments (Strengbach CZO, France). *Earth Surface Processes and Landforms*, 47(14), 3239–3258. <https://doi.org/10.1002/esp.5454>

Aguilar, R. G., Owens, R., & Giardino, J. R. (2020). The expanding role of anthropogeomorphology in critical zone studies in the Anthropocene. *Geomorphology*, 366, 107165. <https://doi.org/10.1016/j.geomorph.2020.107165>

Bao, C., Li, L., Shi, Y., & Duffy, C. (2017). Understanding watershed hydrogeochemistry: 1. Development of RT-flux-PIHM. *Water Resources Research*, 53(3), 2328–2345. <https://doi.org/10.1002/2016WR018934>

Beaujouan, V., Durand, P., & Ruiz, L. (2001). Modelling the effect of the spatial distribution of agricultural practices on nitrogen fluxes in rural catchments. *Ecological Modelling*, 137(1), 93–105. [https://doi.org/10.1016/S0304-3800\(00\)00435-X](https://doi.org/10.1016/S0304-3800(00)00435-X)

Befus, K. M., Sheehan, A. F., Leopold, M., Anderson, S. P., & Anderson, R. S. (2011). Seismic constraints on critical zone architecture, Boulder Creek Watershed, Front Range, Colorado. *Vadose Zone Journal*, 10(3), 915–927. <https://doi.org/10.2136/vzj2010.0108>

Béziat, P., Rivalland, V., Tallec, T., Jarosz, N., Boulet, G., Gentine, P., & Ceschia, E. (2013). Evaluation of a simple approach for crop evapotranspiration partitioning and analysis of the water budget distribution for several crop species. *Agricultural and Forest Meteorology*, 177, 46–56. <https://doi.org/10.1016/j.agrformet.2013.03.013>

Brantley, S. L., McDowell, W. H., Dietrich, W. E., White, T. S., Kumar, P., Anderson, S. P., et al. (2017). Designing a network of critical zone observatories to explore the living skin of the terrestrial Earth. *Earth Surface Dynamics*, 5(4), 841–860. <https://doi.org/10.5194/esurf-5-841-2017>

Braud, I., Chaffard, V., Cousot, C., Galle, S., Juen, P., Alexandre, H., et al. (2020). Building the information system of the French Critical Zone Observatories network: Theia/OZCAR-IS. *Hydrological Sciences Journal*, 67(16), 2401–2419. <https://doi.org/10.1080/02626667.2020.1764568>

Ceschia, E., & Tallec, T., & ICOS Ecosystem Thematic Centre. (2022). Warm winter 2020 ecosystem eddy covariance flux product from Auradé. <https://doi.org/10.18160/BGS5-0X3J>

Chabaux, F., Négrel, P., Gal, F., Viville, D., Ranchoux, C., Van der Woerd, J., et al. (2023). Hard rock aquifer architecture and water circulation levels in the Strengbach critical zone observatory (France). *Comptes Rendus Géoscience*, 1–22. Online first. <https://doi.org/10.5802/crgeos.239>

Chorover, J., Troch, P. A., Rasmussen, C., Brooks, P. D., Pelletier, J. D., Breshars, D. D., et al. (2011). How water, carbon, and energy drive critical zone evolution: The Jemez–Santa Catalina Critical Zone Observatory. *Vadose Zone Journal*, 10(3), 884–899. <https://doi.org/10.2136/vzj2010.0132>

Condon, L. E., Atchley, A. L., & Maxwell, R. M. (2020). Evapotranspiration depletes groundwater under warming over the contiguous United States. *Nature Communications*, 11(1), 873. <https://doi.org/10.1038/s41467-020-14688-0>

Coon, E. T., Moulton, J. D., Kikinzon, E., Berndt, M., Manzini, G., Garimella, R., et al. (2020). Coupling surface flow and subsurface flow in complex soil structures using mimetic finite differences. *Advances in Water Resources*, 144, 103701. <https://doi.org/10.1016/j.advwatres.2020.103701>

Cotel, S., Viville, D., Benarioumlil, S., Ackerer, P., & Pierret, M. C. (2020). Impact of the hydrological regime and forestry operations on the fluxes of suspended sediment and bedload of a small middle-mountain catchment. *Science of the Total Environment*, 743, 140228. <https://doi.org/10.1016/j.scitotenv.2020.140228>

Douinot, A., Tetzlaff, D., Maneta, M., Kuppel, S., Schulte-Bisping, H., & Soulsby, C. (2019). Ecohydrological modelling with ECH<sub>2</sub>O-iso to quantify forest and grassland effects on water partitioning and flux ages. *Hydrological Processes*, 33(16), 2174–2191. <https://doi.org/10.1002/hyp.13480>

Dralle, D. N., Hahm, W. J., Rempe, D. M., Karst, N. J., Thompson, S. E., & Dietrich, W. E. (2018). Quantification of the seasonal hillslope water storage that does not drive streamflow. *Hydrological Processes*, 32(13), 1978–1992. <https://doi.org/10.1002/hyp.11627>

Ferrant, S., Bustillo, V., Burel, E., Salmon-Monviola, J., Claverie, M., Jarosz, N., et al. (2016). Extracting soil water holding capacity parameters of a distributed agro-hydrological model from high resolution optical satellite observations series. *Remote Sensing*, 8(2), 154. <https://doi.org/10.3390/rs8020154>

Ferrant, S., Gascoin, S., Veloso, A., Salmon-Monviola, J., Claverie, M., Rivalland, V., et al. (2014). Agro-hydrology and multi-temporal high-resolution remote sensing: Toward an explicit spatial processes calibration. *Hydrology and Earth System Sciences*, 18(12), 5219–5237. <https://doi.org/10.5194/hess-18-5219-2014>

Flinchum, B. A., Holbrook, W. S., & Carr, B. J. (2022). What do P-wave velocities tell us about the critical zone? *Frontiers in Water*, 3. <https://doi.org/10.3389/frwa.2021.772185>

Fovet, O., Ruiz, L., Gruau, G., Akkal, N., Aquilina, L., Busnot, S., et al. (2018). AgrHyS: An observatory of response times in agro-hydro systems. *Vadose Zone Journal*, 17(1), 1–16. <https://doi.org/10.2136/vzj2018.04.0066>

Gaillardet, J., Braud, I., Hankard, F., Anquetin, S., Bour, O., Dorfliger, N., et al. (2018). OZCAR: The French network of critical zone observatories. *Vadose Zone Journal*, 17(1), 1–24. <https://doi.org/10.2136/vzj2018.04.0067>

Gascuel-Odoux, C., Weiler, M., & Molénat, J. (2010). Effect of the spatial distribution of physical aquifer properties on modelled water table depth and stream discharge in a headwater catchment. *Hydrology and Earth System Sciences*, 14(7), 1179–1194. <https://doi.org/10.5194/hess-14-1179-2010>

Goddéris, Y., & Brantley, S. L. (2013). Earthcasting the future Critical Zone. *Elementa: Science of the Anthropocene*, 1. <https://doi.org/10.12952/journal.elementa.000019>

Guillocheau, F., Brault, N., Thomas, E., & Barbarand, J. (2003). Histoire géologique du Massif Armoricaïn depuis 140 Ma (Crétacé–Actuel). *Bulletin d'Information des Géologues du Bassin de Paris*, 40(1), 13–28.

Gupta, H. V., Kling, H., Yilmaz, K. K., & Martinez, G. F. (2009). Decomposition of the mean squared error and NSE performance criteria: Implications for improving hydrological modelling. *Journal of Hydrology*, 377(1–2), 80–91. <https://doi.org/10.1016/j.jhydrol.2009.08.003>

Habets, F., Boone, A., Champeaux, J. L., Etchevers, P., Franchisteguy, L., Leblois, E., et al. (2008). The SAFRAN-ISBA-MODCOU hydro-meteorological model applied over France. *Journal of Geophysical Research: Atmospheres*, 113(D6). <https://doi.org/10.1029/2007jd008548>



- Keller, B., Herrault, P. A., Schwartz, D., Rixhon, G., & Ertlen, D. (2023). Spatio-temporal dynamics of forest ecosystems revealed by the LIDAR-based characterization of medieval field systems (Vosges Mountains, France). *Anthropocene*, *42*, 100374. <https://doi.org/10.1016/j.anucene.2023.100374>
- Kuffour, B. N. O., Engdahl, N. B., Woodward, C. S., Condon, L. E., Kollet, S., & Maxwell, R. M. (2020). Simulating coupled surface–subsurface flows with ParFlow v3.5.0: Capabilities, applications, and ongoing development of an open-source, massively parallel, integrated hydrologic model. *Geoscientific Model Development*, *13*(3), 1373–1397. <https://doi.org/10.5194/gmd-13-1373-2020>
- Kuppel, S., Tetzlaff, D., Maneta, M. P., & Soulsby, C. (2018a). What can we learn from multi-data calibration of a process-based ecohydrological model? *Environmental Modelling & Software*, *101*, 301–316. <https://doi.org/10.1016/j.envsoft.2018.01.001>
- Kuppel, S., Tetzlaff, D., Maneta, M. P., & Soulsby, C. (2018b). ECH<sub>2</sub>O-iso 1.0: Water isotopes and age tracking in a process-based, distributed ecohydrological model. *Geoscientific Model Development*, *11*(7), 3045–3069. <https://doi.org/10.5194/gmd-11-3045-2018>
- Kuppel, S., Tetzlaff, D., Maneta, M. P., & Soulsby, C. (2020). Critical zone storage controls on the water ages of ecohydrological outputs. *Geophysical Research Letters*, *47*(16), e2020GL088897. <https://doi.org/10.1029/2020gl088897>
- Larsen, M. A., Refsgaard, J. C., Jensen, K. H., Butts, M. B., Stisen, S., & Mollerup, M. (2016). Calibration of a distributed hydrology and land surface model using energy flux measurements. *Agricultural and Forest Meteorology*, *217*, 74–88. <https://doi.org/10.1016/j.agrformet.2015.11.012>
- Lesparre, N., Girard, J. F., Jeannot, B., Weill, S., Dumont, M., Boucher, M., et al. (2020). Magnetic resonance sounding dataset of a hard-rock headwater catchment for assessing the vertical distribution of water contents in the subsurface. *Data in Brief*, *31*, 105708. <https://doi.org/10.1016/j.dib.2020.105708>
- Li, L., Bao, C., Sullivan, P. L., Brantley, S., Shi, Y., & Duffy, C. (2017). Understanding watershed hydrogeochemistry: 2. Synchronized hydrological and geochemical processes drive stream chemostatic behavior. *Water Resources Research*, *53*(3), 2346–2367. <https://doi.org/10.1002/2016WR018935>
- Lozano-Parra, J., Maneta, M. P., & Schnabel, S. (2014). Climate and topographic controls on simulated pasture production in a semiarid Mediterranean watershed with scattered tree cover. *Hydrology and Earth System Sciences*, *18*(4), 1439–1456. <https://doi.org/10.5194/hess-18-1439-2014>
- Lucas, Y., Chabaux, F., Schaffhauser, T., Fritz, B., Ambroise, B., Ackerer, J., & Clément, A. (2017). Hydrogeochemical modeling (KIRMAT) of spring and deep borehole water compositions in the small granitic Ringelbach catchment (Vosges Mountains, France). *Applied Geochemistry*, *87*, 1–21. <https://doi.org/10.1016/j.apgeochem.2017.10.005>
- Maneta, M. P., Pasternack, G. B., Wallender, W. W., Jetten, V., & Schnabel, S. (2007). Temporal instability of parameters in an event-based distributed hydrologic model applied to a small semiarid catchment. *Journal of Hydrology*, *341*(3–4), 207–221. <https://doi.org/10.1016/j.jhydrol.2007.05.010>
- Maneta, M. P., & Silverman, N. L. (2013). A spatially distributed model to simulate water, energy, and vegetation dynamics using information from regional climate models. *Earth Interactions*, *17*(11), 1–44. <https://doi.org/10.1175/2012ei000472.1>
- Maneta, M. P., Soulsby, C., Kuppel, S., & Tetzlaff, D. (2018). Conceptualizing catchment storage dynamics and nonlinearities. *Hydrological Processes*, *32*(21), 3299–3303. <https://doi.org/10.1002/hyp.13262>
- Marçais, J., Derry, L. A., Guillaumont, L., Aquilina, L., & de Dreuzy, J. R. (2022). Dynamic contributions of stratified groundwater to streams controls seasonal variations of streamwater transit times. *Water Resources Research*, *58*(3), e2021WR029659. <https://doi.org/10.1029/2021wr029659>
- Maxwell, R. M., Condon, L. E., Kollet, S. J., Maher, K., Haggerty, R., & Forrester, M. M. (2016). The imprint of climate and geology on the residence times of groundwater. *Geophysical Research Letters*, *43*(2), 701–708. <https://doi.org/10.1002/2015GL066916>
- Molénat, J., Gascuel-Odoux, C., Aquilina, L., & Ruiz, L. (2013). Use of gaseous tracers (CFCs and SF<sub>6</sub>) and transit-time distribution spectrum to validate a shallow groundwater transport model. *Journal of Hydrology*, *480*, 1–9. <https://doi.org/10.1016/j.jhydrol.2012.11.043>
- National Research Council. (2001). *Basic research opportunities in Earth science*. National Academies Press.
- Pasquet, S. (2019). From CRITEX to OZCAR: Geophysical wandering across the French Critical Zone Observatories. In *Geophysical Research Abstracts* (Vol. 21).
- Pasquet, S., Marçais, J., Hayes, J. L., Sak, P. B., Ma, L., & Gaillardet, J. (2022). Catchment-scale architecture of the deep critical zone revealed by seismic imaging. *Geophysical Research Letters*, *49*(13). <https://doi.org/10.1029/2022gl098433>
- Perrin, A. S., Probst, A., & Probst, J. L. (2008). Impact of nitrogenous fertilizers on carbonate dissolution in small agricultural catchments: Implications for weathering CO<sub>2</sub> uptake at regional and global scales. *Geochimica et Cosmochimica Acta*, *72*(13), 3105–3123. <https://doi.org/10.1016/j.gca.2008.04.011>
- Pierret, M. C., Cotel, S., Ackerer, P., Beaulieu, E., Benarioumlil, S., Boucher, M., et al. (2018). The Strengbach catchment: A multidisciplinary environmental sentry for 30 years. *Vadose Zone Journal*, *17*(1), 1–17. <https://doi.org/10.2136/vzj2018.04.0090>
- Pierret, M. C., Viville, D., Dambrine, E., Cotel, S., & Probst, A. (2019). Twenty-five year record of chemicals in open field precipitation and throughfall from a medium-altitude forest catchment (Strengbach-NE France): An obvious response to atmospheric pollution trends. *Atmospheric Environment*, *202*, 296–314. <https://doi.org/10.1016/j.atmosenv.2018.12.026>
- Ponnou-Delaffon, V., Probst, A., Payre-Suc, V., Granouillac, F., Ferrant, S., Perrin, A. S., & Probst, J. L. (2020). Long and short-term trends of stream hydrochemistry and high frequency surveys as indicators of the influence of climate change, agricultural practices and internal processes (Auradé agricultural catchment, SW France). *Ecological Indicators*, *110*, 105894. <https://doi.org/10.1016/j.ecolind.2019.105894>
- Probst, J. L., & Probst, A. (2022). Booklet-Guide of the Auradé Experimental Agricultural Catchment in Auradé (Auradé Catchment, Gascony). Retrieved from <https://hal.science/hal-03760223v1>
- Ranchoux, C., Chabaux, F., Viville, D., Labasque, T., Lucas, Y., Ackerer, J., & Aquilina, L. (2021). Characterization of groundwater circulations in a headwater catchment from an analysis of chemical concentrations, Sr-Nd-U isotope ratios, and CFC, SF<sub>6</sub> gas tracers (Strengbach CZO, France). *Applied Geochemistry*, *131*, 105030. <https://doi.org/10.1016/j.apgeochem.2021.105030>
- Shuai, P., Chen, X., Mital, U., Coon, E. T., & Dwivedi, D. (2022). The effects of spatial and temporal resolution of gridded meteorological forcing on watershed hydrological responses. *Hydrology and Earth System Sciences*, *26*(8), 2245–2276. <https://doi.org/10.5194/hess-26-2245-2022>
- Smith, A. A., Tetzlaff, D., Maneta, M., & Soulsby, C. (2022). Critical zone response times and water age relationships under variable catchment wetness states: Insights using a tracer-aided ecohydrological model. *Water Resources Research*, *58*(4), e2021WR030584. <https://doi.org/10.1029/2021wr030584>
- Sörensen, R., Zinko, U., & Seibert, J. (2006). On the calculation of the topographic wetness index: Evaluation of different methods based on field observations. *Hydrology and Earth System Sciences*, *10*(1), 101–112. <https://doi.org/10.5194/hess-10-101-2006>
- Sprenger, M., & Allen, S. T. (2020). What ecohydrologic separation is and where we can go with it. *Water Resources Research*, *56*(7), e2020WR027238. <https://doi.org/10.1029/2020wr027238>
- Steffen, W., Richardson, K., Rockström, J., Cornell, S. E., Fetzer, I., Bennett, E. M., et al. (2015). Planetary boundaries: Guiding human development on a changing planet. *Science*, *347*(6223), 1259855. <https://doi.org/10.1126/science.1259855>
- Strohmeier, L., Ackerer, P., Belfort, B., & Pierret, M. C. (2022). Local and seasonal climate change and its influence on the hydrological cycle in a mountainous forested catchment. *Journal of Hydrology*, *610*, 127914. <https://doi.org/10.1016/j.jhydrol.2022.127914>



- Taghavi, L., Probst, J. L., Merlina, G., Marchand, A. L., Durbe, G., & Probst, A. (2010). Flood event impact on pesticide transfer in a small agricultural catchment (Montousse at Aurade, southwest France). *International Journal of Environmental Analytical Chemistry*, 90(3–6), 390–405. <https://doi.org/10.1080/03067310903195045>
- Taillefer, F. (1968). Quatre cartes géologiques de la Gascogne gersoise. Carte géologique détaillée de la France: Beaumont-de-Lomagne. Fleurance (1969), Gimont (1969), Lombez (1970) par A. Cavaillé. In *Revue géographique des Pyrénées et du Sud-Ouest, tome 43, fascicule 3, 1972. Le vent d'autan* (pp. 387–390).
- Tallec, T., Béziat, P., Jarosz, N., Rivalland, V., & Ceschia, E. (2013). Crops' water use efficiencies in temperate climate: Comparison of stand, ecosystem and agronomical approaches. *Agricultural and Forest Meteorology*, 168, 69–81. <https://doi.org/10.1016/j.agrformet.2012.07.008>
- Tetzlaff, D., Birkel, C., Dick, J., Geris, J., & Soulsby, C. (2014). Storage dynamics in hydrogeological units control hillslope connectivity, runoff generation, and the evolution of catchment transit time distributions. *Water Resources Research*, 50(2), 969–985. <https://doi.org/10.1002/2013wr014147>
- Trochon, B., Bustillo, V., Caner, L., Pasquet, S., Suc, V., Granouillac, F., et al. (2023). Main water pathways in cultivated clayey calcisols in molassic hills in southwestern France: Towards spatialization of soil waterlogging. *Vadose Zone Journal*, 22(5). <https://doi.org/10.1002/vzj2.20272>
- Viaud, V., Santillán-Carvantes, P., Akkal-Corfini, N., Le Guillou, C., Prévost-Bouré, N. C., Ranjard, L., & Menasseri-Aubry, S. (2018). Landscape-scale analysis of cropping system effects on soil quality in a context of crop-livestock farming. *Agriculture, Ecosystems & Environment*, 265, 166–177. <https://doi.org/10.1016/j.agee.2018.06.018>
- Vidal, J. P., Martin, E., Franchistéguy, L., Baillon, M., & Soubeyrou, J. M. (2010). A 50-year high-resolution atmospheric reanalysis over France with the Safran system. *International Journal of Climatology*, 30(11), 1627–1644. <https://doi.org/10.1002/joc.2003>
- Viville, D., Biron, P., Granier, A., Dambrine, E., & Probst, A. (1993). Interception in a mountainous declining spruce stand in the Strengbach catchment (Vosges, France). *Journal of Hydrology*, 144(1–4), 273–282. [https://doi.org/10.1016/0022-1694\(93\)90175-9](https://doi.org/10.1016/0022-1694(93)90175-9)
- Weill, S., Lesparre, N., Jeannot, B., & Delay, F. (2019). Variability of water transit time distributions at the Strengbach catchment (Vosges Mountains, France) inferred through integrated hydrological modeling and particle tracking algorithms. *Water*, 11(12), 2637. <https://doi.org/10.3390/w11122637>
- White, T., Brantley, S., Banwart, S., Chorover, J., Dietrich, W., Derry, L., et al. (2015). The role of critical zone observatories in critical zone science. In *Developments in earth surface processes* (Vol. 19, pp. 15–78). Elsevier.
- Wyns, R., Baltassat, J. M., Lachassagne, P., Legchenko, A., Vairon, J., & Mathieu, F. (2004). Application of proton magnetic resonance soundings to groundwater reserve mapping in weathered basement rocks (Brittany, France). *Bulletin de la Société Géologique de France*, 175(1), 21–34. <https://doi.org/10.2113/175.1.21>
- Xie, S. P., Deser, C., Vecchi, G. A., Collins, M., Delworth, T. L., Hall, A., et al. (2015). Towards predictive understanding of regional climate change. *Nature Climate Change*, 5(10), 921–930. <https://doi.org/10.1038/nclimate2689>
- Xu, Z., Molins, S., Özgen-Xian, I., Dwivedi, D., Svyatsky, D., Moulton, J. D., & Steefel, C. (2022). Understanding the hydrogeochemical response of a mountainous watershed using integrated surface-subsurface flow and reactive transport modeling. *Water Resources Research*, 58(8), e2022WR032075. <https://doi.org/10.1029/2022WR032075>
- Ziegler, P. A., & Dèzes, P. (2007). Cenozoic uplift of Variscan Massifs in the Alpine foreland: Timing and controlling mechanisms. *Global and Planetary Change*, 58(1–4), 237–269. <https://doi.org/10.1016/j.gloplacha.2006.12.004>